

# The ALMA view of the high redshift relation between supermassive black holes and their host galaxies

A. Pensabene<sup>1,2,3</sup> <sup>\*</sup>, S. Carniani<sup>4</sup>, M. Perna<sup>5,6</sup>, G. Cresci<sup>5</sup>, R. Decarli<sup>2</sup>, R. Maiolino<sup>7,8</sup>, and A. Marconi<sup>3,5</sup>

<sup>1</sup> Dipartimento di Fisica e Astronomia, Alma Mater Studiorum, Università di Bologna, Via Gobetti 93/2, I-40129 Bologna, Italy

<sup>2</sup> INAF-Osservatorio di Astrofisica e Scienza dello Spazio, via Gobetti 93/3, I-40129 Bologna, Italy

<sup>3</sup> Dipartimento di Fisica e Astronomia, Università degli Studi di Firenze, Via G. Sansone 1, I-50019 Sesto Fiorentino (Firenze), Italy

<sup>4</sup> Scuola Normale Superiore, Piazza dei Cavalieri 7, I-56126 Pisa, Italy

<sup>5</sup> INAF-Osservatorio Astrofisico di Arcetri, Largo E. Fermi 2, I-50125 Firenze, Italy

<sup>6</sup> Centro de Astrobiología (CSIC-INTA), Torrejón de Ardoz, 28850 Madrid, Spain

<sup>7</sup> Cavendish Laboratory, University of Cambridge, 19 J. J. Thomson Ave., Cambridge CB3 0HE, UK

<sup>8</sup> Kavli Institute for Cosmology, University of Cambridge, Madingley Road, Cambridge CB3 0HA, UK

Received XXX; accepted YYY

## ABSTRACT

**Context.** The existence of tight correlations between supermassive black holes (BHs) and their host galaxies properties in the local Universe suggests a closely linked evolution. Investigating these relations up to the high redshifts ( $z \gtrsim 6$ ) is crucial to understand the interplay between star-formation and BH growth across the cosmic time and to set constraints on galaxy formation and evolution models. In this work we focus on the relation between BH mass ( $M_{\text{BH}}$ ) and the dynamical mass ( $M_{\text{dyn}}$ ) of the host galaxy.

**Aims.** Previous works suggest an evolution of the  $M_{\text{BH}} - M_{\text{dyn}}$  relation with redshift indicating that BH growth precedes the galaxy mass assembly during their co-evolution at  $z > 3$ . However, dynamical galaxy masses at high redshift are often estimated through the virial theorem thus introducing significant uncertainties. This work aims at studying the  $M_{\text{BH}} - M_{\text{dyn}}$  relation of a sample of  $2 < z < 7$  quasars by constraining their galaxy masses through a full kinematical modelling of the cold gas kinematics thus avoiding all possible biases and effects introduced by the rough estimates usually adopted so far.

**Methods.** For this purpose we retrieved public observations of 72 quasar host galaxies observed in  $[\text{CII}]_{158\mu\text{m}}$  or CO transitions with the Atacama Large Millimeter Array (ALMA). We then selected those quasars whose line emission is spatially resolved and performed a kinematic analysis on ALMA observations. We estimated the dynamical mass of the systems by modelling the gas kinematics with a rotating disc taking into account geometrical and instrumental effects. Our dynamical mass estimates, combined with  $M_{\text{BH}}$  obtained from literature and our own new CIV $\lambda 1550$  observations have allowed us to investigate the  $M_{\text{BH}}/M_{\text{dyn}}$  in the early Universe.

**Results.** Overall we obtained a sample of 10 quasars at  $z \sim 2 - 7$  in which line emission is detected with high SNR ( $\gtrsim 5 - 10$ ) and the gas kinematics is spatially resolved and dominated by ordered rotation. The estimated dynamical masses place 6 out of 10 quasars above the local relation yielding to a  $M_{\text{BH}}/M_{\text{dyn}}$  ratios  $\sim 10\times$  higher than those estimated in low- $z$  galaxies. On the other hand we found that 4 quasars at  $z \sim 4 - 6$  have dynamical-to-BH mass ratios consistent with what is observed in early type galaxies in the local Universe.

**Key words.** Galaxies: evolution – Galaxies: high-redshift – Galaxies: kinematics and dynamics – quasars: supermassive black holes

## 1. Introduction

Supermassive black holes (BHs;  $M_{\text{BH}} \sim 10^6 - 10^{10} M_{\odot}$ ) are believed to reside at the centre of all nearby galaxies and are likely the relics of a past quasar (QSO) activity (e.g., Soltan 1982; Hopkins et al. 2008). Such BHs have likely played a key role in shaping galaxies during their assembly at early epochs with the implication that BH growth and galaxy formation are closely linked (Heckman & Best 2014).

The discovery of the strong correlations (in the local Universe) between the mass of the central black hole ( $M_{\text{BH}}$ ) and the physical properties of host galaxies (e.g., stellar velocity dispersion of the bulge stars, mass of the bulge, etc.; Tremaine et al. 2002; Häring & Rix 2004; see also Kormendy & Ho 2013 for an extensive review and references therein) has been one of the most significant breakthroughs of the past decades and represents a key building block for our understanding of galaxy formation and evolution across the cosmic time. In the framework

of co-evolution between BHs and their host galaxies, the observed local relations are believed to arise from the balance between the energy released by the active galactic nucleus (AGN), which generates galactic-scale outflows expelling gas from the galaxy, and the gravitational potential that keeps the galactic system bound. According to current galaxy evolution models (see e.g.; Lemastra et al. 2010; Sijacki et al. 2015), AGN are able to regulate the star-formation activity in the host and constrain both the final stellar mass and dynamical properties of the galaxy (e.g., Di Matteo et al. 2005; Menci et al. 2008; Hopkins et al. 2008; Kormendy & Ho 2013). Therefore investigating the onset of BH-galaxy relations at high redshift is fundamental to explore the interplay between BH accretion and star formation activity in the host galaxies and to constrain accordingly galaxies formation and evolution models.

In this work we will focus on the relation between BH mass and that of the host galaxy ( $M_{\text{BH}} - M_{\text{gal}}$  relation). The latter has been widely sampled for active and quiescent galaxies in the local Universe ( $z < 1$ ) indicating that BH mass is a defined fraction

<sup>\*</sup> e-mail: antonio.pensabene2@unibo.it

of the bulge stellar mass, i.e.  $M_{\text{BH}} \sim 10^{-3} M_{\text{gal}}$  (e.g. Marconi & Hunt 2003; Häring & Rix 2004). More recently, several groups (Treu et al. 2004, 2007; Walter et al. 2004; Peng et al. 2006a,b; Shields et al. 2006; Woo et al. 2006, 2008; Ho 2007; Decarli et al. 2010; Merloni et al. 2010; Wang et al. 2010; Bennert et al. 2011; Canalizo et al. 2012; Targett et al. 2012; Bongiorno et al. 2014) have attempted to sample this relation beyond the local Universe showing that there are indications for a possible evolution with redshift. In particular these works suggested a parameterisation of the ratio  $\Gamma = M_{\text{BH}}/M_{\text{gal}}$  as a function of redshift,  $\Gamma \propto (1+z)^\beta$ . The published values of  $\beta$  span the range  $0.7 - 2$  (McLure et al. 2006; Bennert et al. 2010, 2011; Decarli et al. 2010; Merloni et al. 2010) with the implication that, at higher redshifts, galaxies host black holes that are more massive than the local counterparts (e.g., a factor of  $\sim 7$  at  $z \sim 3$ ; Decarli et al. 2010). Therefore, during the competitive accretion of matter from the galactic halo that occurred at early epochs, black hole growth possibly must have preceded that of the host galaxy (e.g. Decarli et al. 2010; Bongiorno et al. 2014; Wang et al. 2016).

However, the aforementioned results are affected by observational biases and instrumental limits. The selection of host galaxies revealed at high redshift ( $z > 3$ ), is driven by AGN luminosity, i.e., more massive black holes are preferably selected (Lauer et al. 2007; Vestergaard et al. 2008; Volonteri & Stark 2011; Portinari et al. 2012; Schulze & Wisotzki 2014; Volonteri & Reines 2016). Then, in these sources the luminosity of the central region overwhelms the emission from the host galaxy and the disentangling of the two components is challenging even with high-resolution observations. Since the galaxy stellar mass estimates used to derive the  $M_{\text{BH}} - M_{\text{gal}}$  relation are based upon photometric methods, they are significantly contaminated by light from the central non-stellar source and thus very uncertain. Finally, since the average gas fraction of galaxies increases with the redshift (e.g. Magdis et al. 2017; Tacconi et al. 2018), primordial galaxies may not yet have converted a large fraction of their gas into stars, therefore their stellar mass content may not be a reliable tracer of the total mass (but there are also evidences of luminous QSOs with low gas fraction possibly related to the effect of AGN-driven feedback mechanism, see e.g., Carniani et al. 2017; Kakkad et al. 2017; Brusa et al. 2018; Cresci & Maiolino 2018; Perna et al. 2018). Indeed, the galaxy capability to retain its gas under the influence of AGN activity, is determined by gravitational potential of the whole galaxy traced by the total (dynamical) mass.

The recent advent of ALMA (Atacama Large Millimeter and Sub-Millimeter Array) opened a new era of cold gas observations. Thanks to its unparalleled capability in terms of sensitivity, signal-to-noise ratio (SNR) and angular resolution, it is now possible to spatially resolve the gas kinematics in quasars host galaxies up to the higher redshifts targeting the brightest line emission of the cold gas such as [CII] $_{158\mu\text{m}}$  or CO rotational line transitions with sub-mm spectroscopic observations (see Carilli & Walter 2013; Gallerani et al. 2017, for a comprehensive review). In fact, the emission of radio quiet AGN in the sub-mm band is dominated by the cold gas mass and the dust continuum in their hosts thus allowing observations that are not affected by the non-stellar emission of the central source. Hence, thanks to the efforts of many groups, ALMA has enabled to trace the BH-galaxy relation at very high redshift using dynamical mass estimations of host galaxies (e.g. Wang et al. 2013, 2016; Willott et al. 2013, 2015b; Venemans et al. 2012, 2016, 2017b; Decarli et al. 2017; Trakhtenbrot et al. 2017; Feruglio et al. 2018). The dynamical masses provided in these works are estimated assum-

ing rotating disc geometry and by simply combining the width (FWHM) of the observed line emission, the observed size of the emitting region and the inclination angle of galaxy disc w.r.t. the sky plane. However it is hard to test the basic assumption that the cold atomic/molecular gas of the galaxy is a rotating disc. Furthermore, the disc inclination is calculated from the observed morphology by using the axial ratio of the flux map and is thus affected by significant uncertainties.

In this work we studied a large sample ( $\sim 70$ ) of  $2 < z < 7$  quasars observed by ALMA targeting the [CII] $_{158\mu\text{m}}$  atomic fine-structure line or the CO rotational line emission, which we exploited to trace the morphology and kinematics of quasar host galaxies. Overall we identified ordered rotational motion in a sample of 10 quasars (which high SNR allowed spatially resolved analysis). By carefully modelling the kinematics with rotating discs we were able to measure their host galaxy dynamical mass, at variance with previous work where rough estimates are usually adopted. Our dynamical mass measurements, combined with  $M_{\text{BH}}$  estimates obtained from the literature allowed to trace the evolution of  $M_{\text{BH}} - M_{\text{gal}}$  relation and to study the trend of  $\Gamma = M_{\text{BH}}/M_{\text{gal}}$  across the cosmic time.

The paper is organised as follow:

- Sect. 2: we outline our starting sample and the data reduction performed on the raw data.
- Sect. 3: we illustrate the methods of data analysis to retrieve the information on morphology and kinematics of the host galaxies.
- Sect. 4: we illustrate the kinematical model used to measure the galaxy dynamical mass.
- Sect. 5: we obtain the BH masses from the literature and from LBT data.
- Sect. 6: we recap the different sub-selections of the starting sample that occurred during this work.
- Sect. 7: we compare our dynamical mass estimates with previous similar studies and discuss the uncertainties on our measurements. Then, we investigate limits of validity of the assumptions.
- Sect. 8: we present the  $M_{\text{BH}} - M_{\text{dyn}}$  relation and the trend of  $M_{\text{BH}}/M_{\text{dyn}}$  ratio across cosmic time.
- Sect. 9: we discuss our results comparing them with previous work. We also discuss how possible additional uncertainties and biases could affect the results both from observational and theoretical point of view. Finally, we compute the virial masses of our final sample and we compare them with our dynamical mass estimates.
- Sect. 10: we draw our conclusions.

Throughout the paper we assume a standard  $\Lambda$ CDM cosmology with  $H_0 = 69.3 \text{ km s}^{-1} \text{ Mpc}^{-1}$ ,  $\Omega_m = 0.287$ ,  $\Omega_\Lambda = 1 - \Omega_m$  from Hinshaw et al. (2013).

## 2. ALMA data selection and reduction

We started by collecting all [CII] $_{158\mu\text{m}}$  and CO( $J \rightarrow J-1$ ) (rotational quantum number  $J = 4, 3$ ) observations of  $z > 1.5$  QSOs on the ALMA data archive public as of June 2017 for a total of 72 QSOs in the redshift range  $1.5 < z < 7.1$ .

Different ALMA bands were involved according to the atomic/molecular transition targeted and the redshift of the sources. The collected data were calibrated using the ALMA pipeline in the Common Astronomy Software Applications, CASA (McMullin et al. 2007), by executing the appropriate ALMA calibration scripts corresponding to each specific observation. Continuum images were produced for each quasar from

**Table 1.** List of 32 QSOs revealed with emission line detection significant at  $\geq 3\sigma$  and related information about the ALMA observing project.

No.	Object ID	R.A. (J2000)	DEC. (J2000)	$z_{\text{cat}}^a$	Observed line	Flags [rot, $\beta$ , $M_{\text{BH}}$ ] <sup>b</sup>
1	CXOCDFS J0332-2746	03 <sup>h</sup> 32 <sup>m</sup> 31 <sup>s</sup> .46	−27°46′23″.18	2.2234	CO(4-3)	r, u, −
2	VHS J2101-5943	21 <sup>h</sup> 01 <sup>m</sup> 19 <sup>s</sup> .5	−59°43′45″	2.313	CO(3-2)	r, b, a
3	ULAS J1234+0907	12 <sup>h</sup> 34 <sup>m</sup> 27 <sup>s</sup> .52	+09°07′54″.2	2.503	CO(3-2)	u, −, −
4	ULAS J2315+0143	23 <sup>h</sup> 15 <sup>m</sup> 56 <sup>s</sup> .23	+01°43′50″.38	2.560	CO(3-2)	r, u, −
5	ULAS J0123+1525	01 <sup>h</sup> 23 <sup>m</sup> 12 <sup>s</sup> .52	+15°25′22″.52	2.629	CO(3-2)	u, −, −
6	SDSS J1328-0224	13 <sup>h</sup> 28 <sup>m</sup> 53 <sup>s</sup> .65	−02°24′41″.79	4.62271	[CII]	r, c, e
7	SDSS J0923+0247	09 <sup>h</sup> 23 <sup>m</sup> 03 <sup>s</sup> .52	+02°47′39″.68	4.66307	[CII]	r, c, e
8	SDSS J0331-0741	03 <sup>h</sup> 31 <sup>m</sup> 19 <sup>s</sup> .66	−07°41′43″.16	4.72426	[CII]	r, u, −
9	SDSS J0129-0035	01 <sup>h</sup> 29 <sup>m</sup> 58 <sup>s</sup> .5	−00°35′39″	5.780	[CII]	r, l, a
10	SDSS J1044-0125	10 <sup>h</sup> 44 <sup>m</sup> 33 <sup>s</sup> .04	−01°25′02″.07	5.800	[CII]	r, c, a
11	SDSS J1306+0356	13 <sup>h</sup> 06 <sup>m</sup> 08 <sup>s</sup> .25	+03°56′26″.33	6.016	[CII]	r, c, e
12	SDSS J2310+1855	23 <sup>h</sup> 10 <sup>m</sup> 38 <sup>s</sup> .88	+18°55′19″.72	6.040	[CII]	r, c, e
13	SDSS J0842+1218	08 <sup>h</sup> 42 <sup>m</sup> 29 <sup>s</sup> .43	+12°18′50″.48	6.055	[CII]	u, −, −
14	SDSS J2054-0005	20 <sup>h</sup> 54 <sup>m</sup> 06 <sup>s</sup> .49	−00°05′14″.57	6.062	[CII]	r, c, a
15	[WMH2013] 05	02 <sup>h</sup> 26 <sup>m</sup> 27 <sup>s</sup> .03	−04°52′38″.3	6.068	[CII]	u, −, −
16	CFHQS J2100-1715	21 <sup>h</sup> 00 <sup>m</sup> 54 <sup>s</sup> .62	−17°15′22″.5	6.09	[CII]	u, −, −
17	DES J0454-4448	04 <sup>h</sup> 54 <sup>m</sup> 01 <sup>s</sup> .79	−44°48′31″.1	6.100	[CII]	u, −, −
18	CFHQS J1509-1749	15 <sup>h</sup> 09 <sup>m</sup> 41 <sup>s</sup> .8	−17°49′27″	6.120	[CII]	u, −, −
19	ULAS J1319+0950	13 <sup>h</sup> 19 <sup>m</sup> 11 <sup>s</sup> .29	+09°50′51″.34	6.130	[CII]	r, l, e
20	PSO J065-26	04 <sup>h</sup> 21 <sup>m</sup> 38 <sup>s</sup> .05	−26°57′15″.60	6.14	[CII]	u, −, −
21	[CLM2003] J0228-04161	02 <sup>h</sup> 28 <sup>m</sup> 02 <sup>s</sup> .97	−04°16′18″.3	6.17	[CII]	u, −, −
22	PSO J308-21	20 <sup>h</sup> 32 <sup>m</sup> 10 <sup>s</sup> .00	−21°14′02″.4	6.2342	[CII]	r, b, u
23	VIKING J1152+0055	11 <sup>h</sup> 52 <sup>m</sup> 21 <sup>s</sup> .27	+00°55′36″.6	6.37	[CII]	u, −, −
24	PSO J159-02	10 <sup>h</sup> 36 <sup>m</sup> 54 <sup>s</sup> .19	−02°32′37″.94	6.38	[CII]	u, −, −
25	PSO J183+05	12 <sup>h</sup> 12 <sup>m</sup> 26 <sup>s</sup> .98	+05°05′33″.49	6.4386	[CII]	r, l, u
26	PSO J167-13	11 <sup>h</sup> 10 <sup>m</sup> 33 <sup>s</sup> .98	−13°29′45″.6	6.508	[CII]	r, c, e
27	PSO J231-20	15 <sup>h</sup> 26 <sup>m</sup> 37 <sup>s</sup> .84	−20°50′00″.8	6.58651	[CII]	r, u, −
28	VIKING J0305-3150	03 <sup>h</sup> 05 <sup>m</sup> 16 <sup>s</sup> .92	−31°50′56″.0	6.605	[CII]	r, c, e
29	VIKING J1048-0109	10 <sup>h</sup> 48 <sup>m</sup> 19 <sup>s</sup> .08	−01°09′40″.29	6.661	[CII]	u, −, −
30	VIKING J0109-3047	01 <sup>h</sup> 09 <sup>m</sup> 53 <sup>s</sup> .13	−30°47′26″.3	6.750	[CII]	r, u, −
31	VIKING J2348-3054	23 <sup>h</sup> 48 <sup>m</sup> 33 <sup>s</sup> .34	−30°54′10″.0	6.890	[CII]	u, −, −
32	ULAS J1120+0641	11 <sup>h</sup> 20 <sup>m</sup> 01 <sup>s</sup> .48	+06°41′24″.3	7.080	[CII]	u, −, −

No. <sup>c</sup>	ALMA ID	P.I. <sup>d</sup>	$\sigma_{\text{line}}^e$ (mJy/beam)	$\theta_{\text{beam}}^f$ (″)	Ref. <sup>g</sup>	No. <sup>c</sup>	ALMA ID	P.I. <sup>d</sup>	$\sigma_{\text{line}}^e$ (mJy/beam)	$\theta_{\text{beam}}^f$ (″)	Ref. <sup>g</sup>
1	2015.1.00228.S	GP	0.60	1.66	P17	17	2015.1.01115.S	FW	1.25	1.24	V18
2	2015.1.01247.S	MB	0.68	5.39	B17	18	2015.1.01115.S	FW	1.10	1.04	D18
3	2015.1.01247.S	MB	1.20	2.65	B17	19	2012.1.00240.S	RW	0.62	0.22	J17
4	2015.1.01247.S	MB	0.73	2.22	B17	20	2015.1.01115.S	FW	1.28	0.82	D18
5	2015.1.01247.S	MB	0.74	2.58	B17	21	2013.1.00815.S	CW	0.60	0.39	W15
6	2013.1.01153.S	PL	0.71	0.44	T17	22	2016.A.00018.S	RD	0.54	0.27	D17
7	2013.1.01153.S	PL	0.69	0.45	T17	23	2015.1.01115.S	FW	1.21	0.92	D18
8	2013.1.01153.S	PL	1.60	0.34	T17	24	2015.1.01115.S	FW	1.20	0.89	D18
9	2012.1.00240.S	RW	0.66	0.17	–	25	2016.1.00544.S	EB	0.64	0.25	–
10	2011.0.00206.S	RW	1.84	0.48	W13	26	2015.1.00606.S	CW	0.58	0.63	W17
11	2015.1.01115.S	FW	1.35	0.83	D18	27	2015.1.01115.S	FW	1.37	0.97	D17
12	2011.0.00206.S	RW	1.39	0.57	W13	28	2015.1.00399.S	BV	0.51	0.19	–
13	2015.1.01115.S	FW	1.35	0.93	D17	29	2015.1.01115.S	FW	1.01	0.98	D18
14	2011.0.00206.S	RW	1.81	0.45	W13	30	2012.1.00882.S	BV	1.45	0.36	V16
15	2013.1.00815.S	CW	0.58	0.37	W15	31	2012.1.00882.S	BV	1.88	0.42	V16
16	2015.1.01115.S	FW	1.30	0.62	D17	32	2012.1.00882.S	BV	0.67	0.20	V17

**Notes.** *Top table:* <sup>a</sup>Redshift values retrieved from SIMBAD Astronomical Database (<http://simbad.u-strasbg.fr/simbad/>). <sup>b</sup>The flags provide information on kinematics (rot), disc inclination angle ( $\beta$ ) as resulting by our kinematical modelling, and black hole mass ( $M_{\text{BH}}$ ) as follows: [rot]: unresolved (u) or resolved (r) kinematics. [ $\beta$ ]: unconstrained (u) or constrained (c) disc inclination angle, lower limit (l), bimodal distribution (b). [ $M_{\text{BH}}$ ]: unavailable in the literature (u), single-epoch virial mass estimated in this work (e) or value retrieved the literature (a). *Bottom table:* <sup>c</sup>Identification numbers (No.) refer to that of the top table. <sup>d</sup>Principal investigator of the project: BV (Venemans, B.), CW (Willott, C.), EB (Bañados, E.), FW (Walter, F.), GP (Popping, G.), MB (Banerji, M.), PL (Lira, P.), RD (Decarli, R.), RW (Wang, R.). <sup>e</sup>Line sensitivity over 10 km s<sup>−1</sup>. <sup>f</sup>Angular resolution. <sup>g</sup>References: V16, V17, V18 (Venemans et al. 2016, 2017b, 2018), B17 (Banerji et al. 2017), D17, D18 (Decarli et al. 2017, 2018), J17 (Jones et al. 2017) P17 (Popping et al. 2017), T17 (Trakhtenbrot et al. 2017), W13 (Wang et al. 2013), W15, W17 (Willott et al. 2015b, 2017).



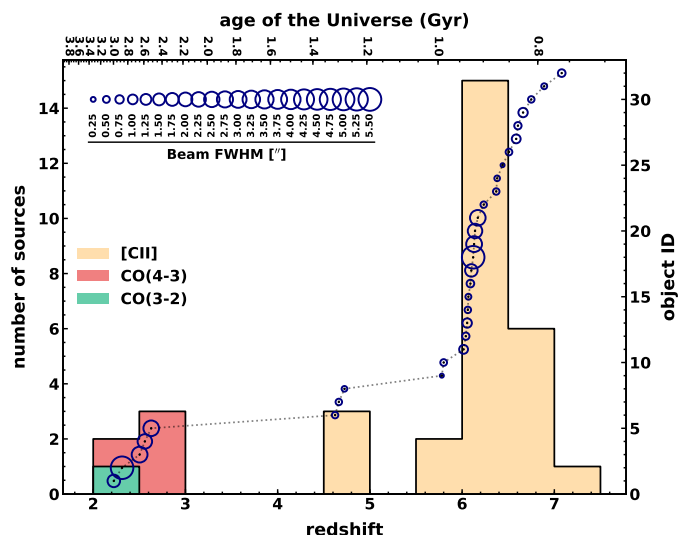


**Fig. 1.** The redshift distribution of 32 QSOs listed in Table 1. The histograms colours indicate the emission line detected in the ALMA data. The figure also shows the sample cumulative redshift distribution (dotted line and right axis). Individual sources are marked with blue circles which sizes are proportional to the ALMA synthesised beam FWHM.

the calibrated visibilities, by combining the line free channels from all spectral windows in multifrequency synthesis mode using the CASA task *tclean* and *briggs* weighting scheme (with robustness parameter  $R = 0.5$ ) to maximise both the signal-to-noise ratio and angular resolution. The line-free channels were determined by inspecting the visibilities in all the frequency sidebands. For those quasars in which the FIR line is not detected, we selected the line-free channel by adopting a line width of  $300 \text{ km s}^{-1}$  and the redshift from literature.

These same channels were also used to produce a UV plane model by fitting the continuum emission with a zeroth order polynomial<sup>1</sup> and then was subtracted from the spectral windows containing the line using the CASA task *uvcontsub*. The continuum subtracted line visibilities were then imaged using *tclean*. In order to recover all the information within the resolution element, the pixel size is commonly set to  $\sim B_{\text{min}}/7$ , where  $B_{\text{min}}$  is the minor FWHM of ALMA synthesised beam. Therefore, we obtained cubes with a typical pixel size of  $0.025'' - 0.05''$  and with spectral bin width set to  $40 - 70 \text{ km/s}$ . Self-calibration was attempted but showed no additional improvement for almost all observations and was not used for the final cubes. Finally, both continuum images and the line cubes were corrected for the primary beam response.

Among these observations, we selected those cubes in which the line detection is significant ( $\geq 3\sigma$ ). This first selection reduced the sample to 32 QSOs at  $2.2 < z < 7.1$  on which we performed all the analysis described in the following sections. Different sub-selections occurred at each step of the analysis (see Sect. 6) and the final sample is composed by only 10 sources for which we obtained constraints on the host galaxy dynamical mass. We thus picked from the archive deeper observations for this final sub-sample of sources that have become public while the work was in progress (by the end of February 2018). In Table 1 we list the starting sample of 32 objects and the characteristics of the observations including the aforementioned deeper

observations for the final sub-sample. The distribution of redshifts of our quasars is illustrated in Fig. 1.

### 3. Methods of data analysis

Our goal is to measure the dynamical mass of our sample of host galaxies (listed in Table 1) by modelling the gas kinematics as traced by  $[\text{CII}]_{158\mu\text{m}}$  or CO line emission with rotating discs. Therefore, in order to obtain the kinematical maps we performed a spaxel-by-spaxel fit of the emission line profile by adopting a single Gaussian model with three free parameters: the amplitude  $A$ , the central frequency  $\nu_{\text{obs}}$  and the standard deviation  $\sigma$ . For this purpose we designed an algorithm to achieve a robust residuals minimisation in each pixel. Since the beam smearing affects the observed emission, we expect that the spatial shape of the line changes smoothly from a pixel to the adjacent one and the signal-to-noise ratio decreases as a function of the distance from the centre of the galaxy. The underlying idea of the procedure is that of performing the line fit subsequently in all spaxels starting from the central pixel and moving away following a spiral-like path. The basic operations are:

1. performing a 2D Gaussian fit on the continuum image and define the central spaxel;
2. extracting the spectrum from the central spaxel and compute a 1D Gaussian line fit in which the starting points are properly chosen inspecting the line shape. We use the minimum chi-square method to estimate the best-fitting parameters;
3. following a spiral-like path select the next spaxel, extract the spectrum, and perform a 1D Gaussian line fit by using the best-fitting results from the neighbour spaxels as starting points for the spectral fit;
4. keep on repeating the step 3 for the consecutive spaxel until the end of the spiral-like path.

The result of the fit in each pixels is accepted or rejected on the basis of criteria illustrated in Sect. 3.2, while the stopping criteria to break the entire fitting procedure can be fixed setting the dimension  $d$  of the spiral path, i.e. the distance from the central pixel. In the case of our datacubes, a typical values of  $d \sim 20 - 25$  pixels ( $\sim 0.5'' - 1.25''$  depending on the pixels size, see Sect. 2) it is turned out to be adequate to fit the line in all the emitting region with a total of  $\sim 1200 - 2000$  pixels analysed for each sources. This fitting strategy enables a more robust minimisation compared with using a unique set of initial guess parameters for all the pixels thus avoiding numerical problems arising from wrong choices of the starting-points. Finally, we retrieve the information about the line together with the uncertainties on each spectral channel of the cube by measuring the *rms* of the noise ( $r_{\nu}$ ) over a wide spatial region where no emission is detected.

#### 3.1. Integrated spectra and derived quantities

We obtain the integrated spectra of all the sources by adding all the fitted spectra in spaxels selected on the base of criteria illustrated in Sect. 3.2 (e.g., Fig. 3, see also Appendix E). Then, the resulting integrated spectrum was fitted using a Monte Carlo method in order to estimate the redshift uncertainty. First we collected a large number (e.g., 2000) of different integrated spectra obtained by adding in each channel of the original spectrum, a random value extracted from a normal distribution defined by a zero mean and a standard deviation equal to the corresponding *rms* in that channel ( $r_{\nu}$ ). Then, we performed the fit of each spectrum with a single Gaussian and we estimate the redshift of the

<sup>1</sup> For a typical SNR  $\sim 60 - 100$  over a bandwidth of 4 GHz in ALMA band 3, the continuum emission are well described by a zeroth-order polynomial within the uncertainties.



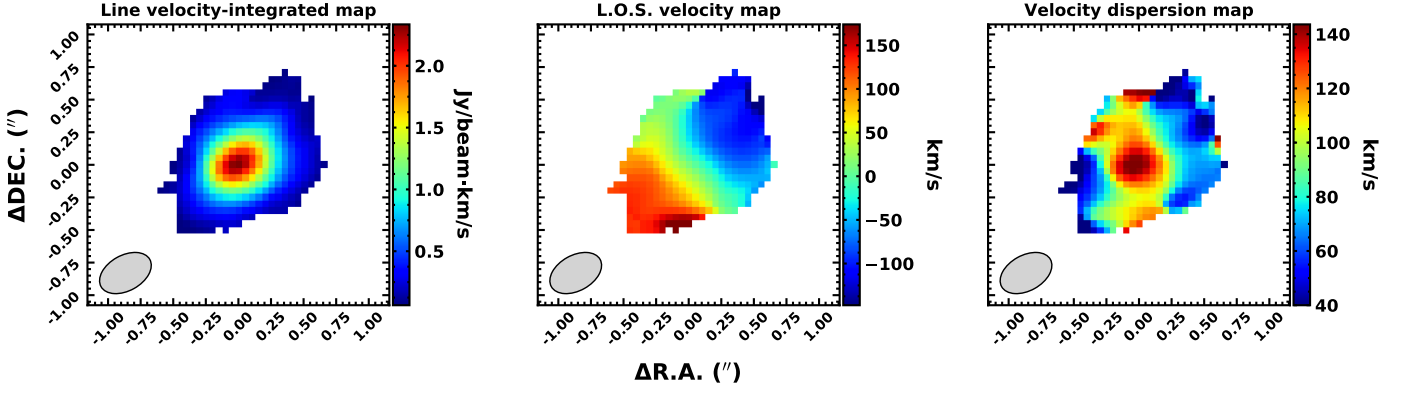


**Fig. 2.** Observed maps of the SDSS J0923+0247. *From left panel to right:* flux map, velocity map and velocity dispersion map along the line of sight. At the bottom left corner of each panel we report the ALMA synthesised beam FWHM. The coordinates indicate offsets w.r.t. the map centre.

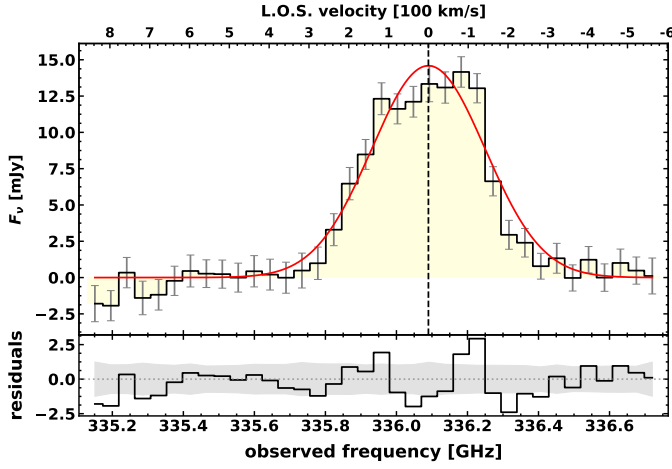


**Fig. 3.** Integrated spectrum of the source SDSS J0923+0247. *Top panel:* The observed data is shown in light yellow with error bars in grey ( $rms$  in each channel). The red solid curve is the best-fit Gaussian model. The velocity scale (top axes) is referred to the central frequency of the best fit. *Bottom panel:* the fit residuals ( $model-data$ ), the grey filled area shows the  $rms$  along the spectral axis.

line as  $\nu_{obs} = \nu_{rest}/(1+z)$ , where  $\nu_{obs}$  is the mean of the Gaussian model and  $\nu_{rest}$  is the line rest-frame frequency. Finally, all the estimates of  $z$  obtained with this method were histogrammed and its distribution was fitted with a Gaussian model. We finally assume the mean and the standard deviation of the best-fit model as the best value of redshift and its uncertainty respectively. In addition, the fit of integrated spectra allow us to determine the line FWHM and flux. In Appendix A we use these quantities to derive the line luminosity, the [CII] mass ( $M_{[CII]}$ ), the total gas mass ( $M_{gas}$ ) and the star formation rate (SFR) of the quasar host galaxies.

### 3.2. Flux, velocity and velocity dispersion maps

The cube fitting procedure provide the best-fit values of the Gaussian parameters ( $A, \nu_{obs}, \sigma$ ) in each pixel. We use these values to obtain the line-integrated, velocity and the velocity dispersion maps along the line of sight (LOS).

In order to produce the maps, among all the spaxels in which we performed the line fit, we select those satisfying the following conditions:

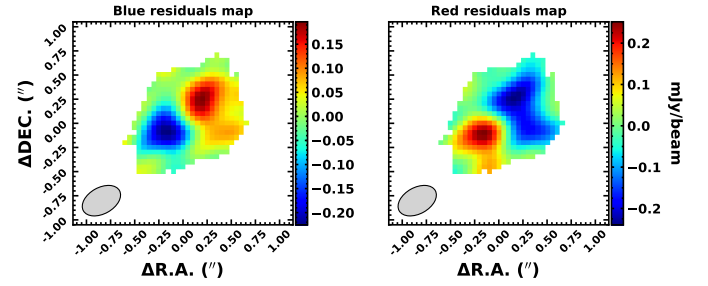


**Fig. 4.** Red and blue residuals maps of SDSS J0923+0247. This test reveals spatially resolved kinematics consistent to what we would expect from a rotating disc.

1. the peak of the best fitting Gaussian is  $\geq 1.5 \times rms$  in the corresponding channel .
2. the percentage relative error on the flux value is  $\leq 50\%$ .

Condition 1 represents the signal-to-noise cut-off we used to reject pixels in which the line emission is not clearly detected. However, in case of poor signal-to-noise ratio, the fit process possibly fails resulting in a bad Gaussian model for which the condition no. 1 could be still satisfied. Thus we also imposed the condition no. 2 in order to avoid this kind of effect and to consequently reject the corresponding pixels when producing the maps.

We also manually masked bad pixels far away from the galaxy centre which are clearly associated to spikes of noise. Finally, we obtained error maps using the uncertainties on the best-fit Gaussian model parameters of each pixel. As an example, in Fig. 2 we report the maps obtained from the continuum-subtracted cube of SDSS J0923+0247 (see also Appendix E).

### 3.3. Red and blue residuals maps

The angular resolution may not be high enough to spatially resolve the rotation of the emitting gas in host galaxies. In order to assess if the kinematics is spatially resolved or not, we performed the same analysis computed by [Carniani et al. \(2013\)](#) for ALMA [CII] observations of a QSO at  $z = 4.7$ . We replicate the spaxel-by-spaxel fit of continuum-subtracted cubes with a single Gaussian component, using the amplitude ( $A$ ) as the only free parameter and fixing the values of  $\nu_{obs}$  and  $\sigma$  to the best values obtained from the fit of the integrated spectrum (see Sect. 3.1). Then, we compute the residuals of fits in each chan-

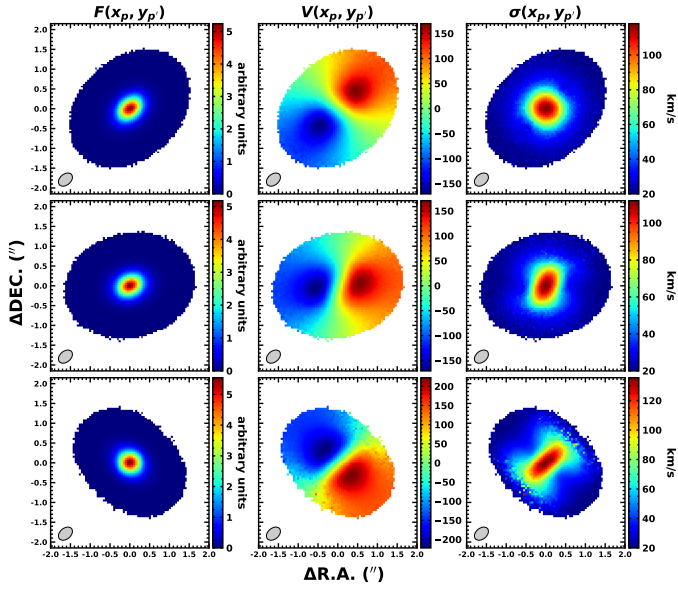


**Fig. 5.** Simulated maps obtained with the kinematical model for a galaxy thin disc with an exponential brightness profile defined by a scale radius  $R_D = 0.125''$  and dynamical mass  $M_{\text{dyn}} = 5.0 \times 10^{10} M_{\odot}$ . The flux, velocity and velocity dispersion maps along the LOS are indicated by  $F(x_p, y_p)$ ,  $V(x_p, y_p)$ ,  $\sigma(x_p, y_p)$  respectively. From the top to the bottom panel: disc inclination and the position angle ( $\beta, \gamma$ ) are respectively equal to  $(40, -45)$  deg,  $(40, 0)$  deg,  $(60, 45)$  deg. The other parameters defining the model are: the FWHM of the synthesised beam  $(0.4'' \times 0.275'')$ , the position angle of the beam ( $B_{\text{PA}} = -50$  deg), the FWHM of the LSF ( $\sigma_{\text{LSF}} = 20 \text{ km s}^{-1}$ ), the bin size  $(0.05'' \times 0.05'')$  and the angular radius of the disc ( $R = 1.25''$ ). The number of clouds used in this model is  $N_p = 7.5 \times 10^6$ .

nel, i.e. *data – model*, and we obtain two maps by collapsing all channels in the blue-shifted and red-shifted (w.r.t. the central frequency) side of the residual spectrum. If the kinematics is consistent with a spatially-resolved rotating disc, we expect that blue and red residual maps show two symmetric lobes: a positive and negative lobe at the opposite side with respect to the map centre (e.g., as shown in Fig. 4). Otherwise, if rotation is not resolved then we expect a random distribution of negative and positive residuals on both the maps. After performing this test on the 32 objects listed Table 1, we conclude that 14 of them ( $\sim 45\%$ ) show no evidence of spatially-resolved kinematics. We thus definitely exclude them as a part of the final sample (see Sect. 6 for a summary of sample sub-selections). In Sect. 7.4 we investigate biases possibly occurring in excluding these objects.

#### 4. Kinematical modelling

In Sect. 3 we obtained all the information about galaxies morphology (line-integrated maps) and kinematics (velocity and velocity dispersion maps). In order to measure the dynamical masses of the host galaxies, we designed a kinematical model to perform 2D fit of the maps. Therefore, we assumed that:

1. The observed line emission (i.e.,  $[\text{CII}]_{158\mu\text{m}}$  or CO transition) traces cold gas distributed in a rotating thin disc.
2. The gas mass surface density  $\Sigma(r)$ , is an exponential distribution that also tracks the distribution of surface brightness  $I(r)$ , i.e.:

$$\Sigma(r) \propto I(r) = I_0 \exp(-r/R_D), \quad (1)$$

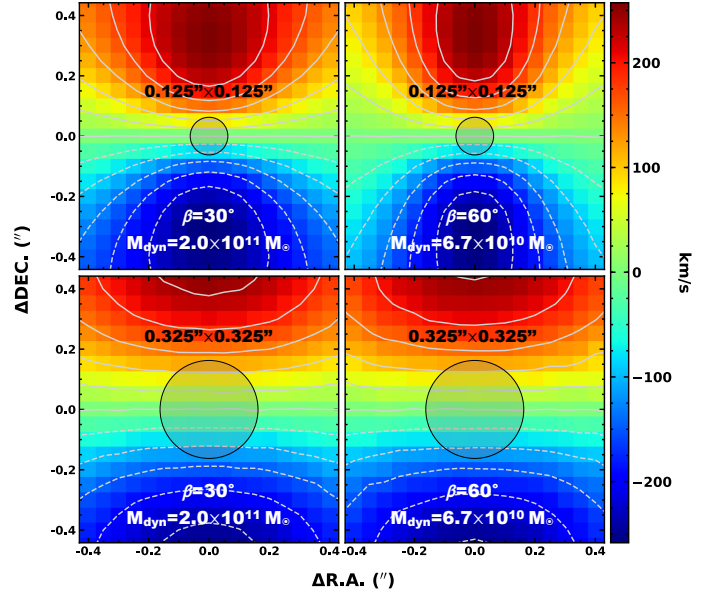


**Fig. 6.** Simulated velocity field corresponding to four different couples of inclination angle  $\beta$  and dynamical mass  $M_{\text{dyn}} = 5.0 \times 10^{10} / \sin^2 \beta$ . Increasing the dimension of the beam FWHM (shadowed area), the iso-velocity curves are increasingly smoothed and different configuration of the disc appear almost indistinguishable. The simulated maps are obtained with the kinematical model for a galaxy thin disc with  $R_D = 0.125''$ ,  $\gamma = -90$  deg. The other parameters defining the model are set equal to the model of Fig. 5.

where  $I_0$  is a normalisation constant and  $R_D$  is the scale radius.

3. The galaxy stellar mass is distributed as the gas mass component (Eq. 1).
4. The contribution of the dark matter is negligible.

Under these assumptions Freeman (1970) has shown that the corresponding circular velocity is given by:

$$V^2(r) = 4\pi G \Sigma_0 R_D y^2 [I_0(y) \mathcal{K}_0(y) - I_1(y) \mathcal{K}_1(y)], \quad (2)$$

where  $I$  and  $\mathcal{K}$  are the modified Bessel functions evaluated at  $y = r/2R_D$  and  $\Sigma_0$  is the normalisation constant of the mass distribution that accounts for both gas and stars contribution.

The total mass of the disc, i.e. the dynamical mass of the galaxy ( $M_{\text{dyn}}$ ), is thus obtained by integrating the mass surface density over all the radii;  $M_{\text{dyn}} = 2\pi R_D^2 \Sigma_0$ . By inserting this expression in the Eq. 2 we can relate the total dynamical mass with the velocity curve:  $V^2(r) = 2(M_{\text{dyn}}/R_D) G y^2 [I_0(y) \mathcal{K}_0(y) - I_1(y) \mathcal{K}_1(y)]$ . Therefore, by estimating  $R_D$  from the flux map we can infer the galaxy dynamical mass by performing 2D fit of the velocity field.

##### 4.1. Details on the kinematical model and the strategy of the analysis

The kinematical model is calculated making use of Monte Carlo methods. At first, the 3D space is randomly filled with  $N \gg 1$  point-like sources uniformly distributed in a thin disc. Each source represents a "cloud" that contributes with a unit of flux in the computation of the total observed flux. Then, the 3D disc model is projected on the sky plane and convolved with the appropriate instrumental point spread function (PSF) and line spread function (LSF) of the observation. Thus, the flux map, the flux-weighted velocity map and the velocity dispersion map are

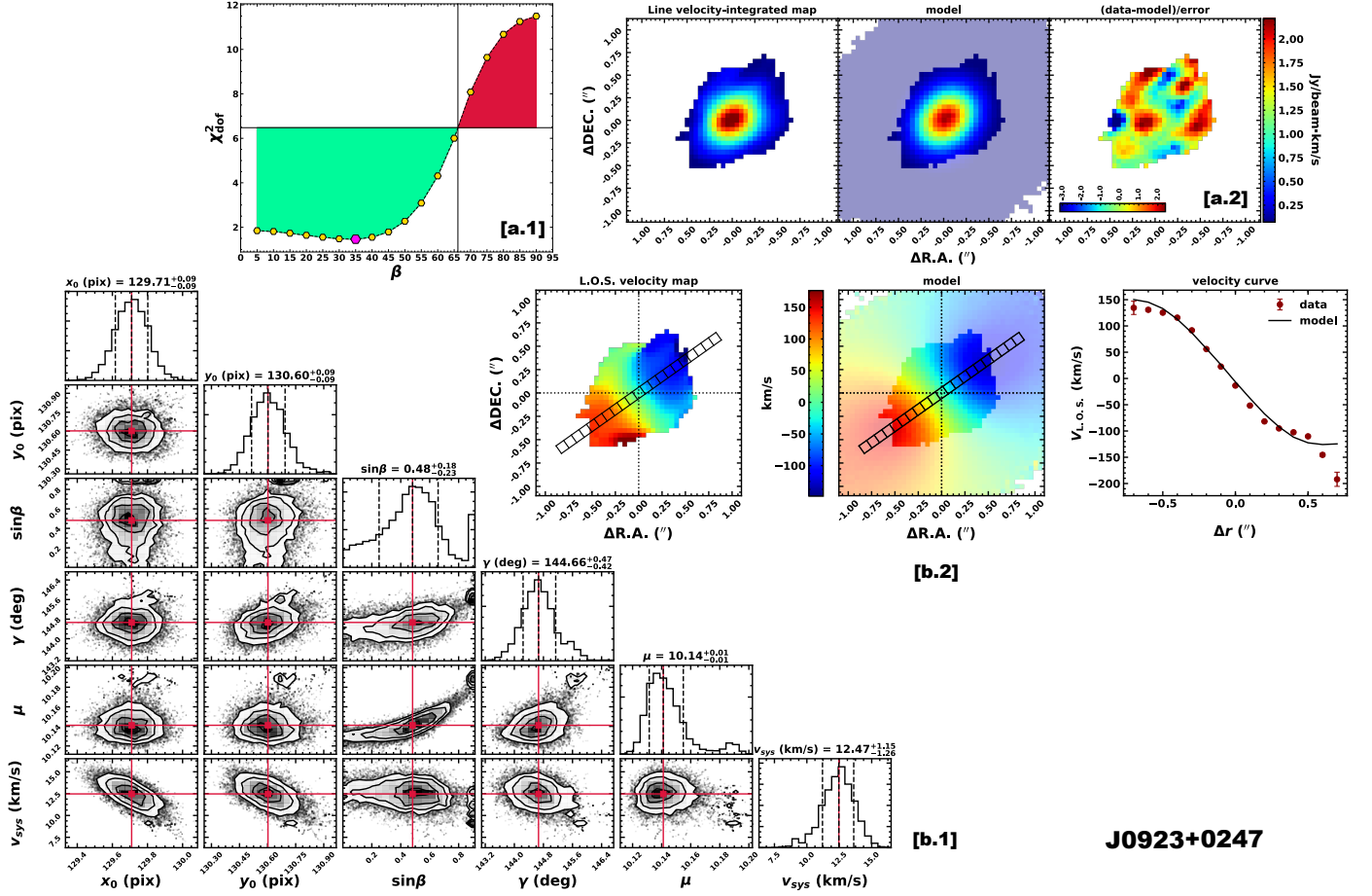


**Fig. 7.** The figure shows the kinematical modelling performed on SDSS J0923+0247. The upper panels [a.1] & [a.2] show the fit result of the flux map while the bottom panels [b.1] & [b.2] show the result of the 2D velocity field fit. [a.1]: the curve of  $\chi^2$  minima as a function of the disc inclination (see Sect. 4.2 for details). The magenta hexagon indicates the absolute minimum ( $= 35$  deg) of  $\chi_m(\beta)$ . The green area (see Sect. 4.3 for the definition) indicates the allowed inclination values used as a prior in performing 2D velocity field fit. [a.2]: 2D best fit model of the flux map. From left to right we report the observed map, the model and the residuals ( $[data-model]/error$ ). [b.1]: the posterior probability distributions of the free parameters in 2D velocity field fit retrieved with the MCMC algorithm with the best values and their uncertainties. [b.2]: 2D best fit model of the kinematical map. From left to right we report the observed velocity map, the model and the velocity curves extracted from a long-slit of 2 pixel width aligned with the line of nodes. The slit is superimposed on maps; red circles and solid black lines in the right panel indicate the observed flux-weighted velocity values in each bin of the slit and the model respectively.

obtained through 2D weighted histograms by using as bin width the pixel size of the corresponding observed map. By properly choosing the weights we can set the flux contribution of each cloud forming the model in order to reproduce any brightness (density) and velocity profile. We set the weights in order to create an exponential thin disc defined by Eq. 1 and Eq. 2. As an example, in Fig. 5 we show the simulated flux, velocity and velocity dispersion maps obtained with our kinematical model in three different geometrical configurations.

In order to recover the galaxies dynamical masses, we basically adopt the same method used in Cresci et al. (2009) and Carniani et al. (2013) that is briefly explained here:

1. We first performed a 2D fit of the observed flux map using a thin disc model with an exponential brightness profile and we recover the best value of scale radius  $R_D$  (see Eq. 1);
2. By using the best value of  $R_D$  obtained in step 1, we compute the velocity field of our disc model accordingly with Eq. 2 and we perform a 2D fit of the LOS velocity map thus recovering the best estimate of  $M_{dyn}$ .

#### 4.2. Estimation of $R_D$ : 2D fit of the flux maps

Following the method illustrated in the previous Sect. 4.1, we first estimate the scale radius  $R_D$  on the 18 flux maps of the sources with spatially-resolved kinematics. The typical angular extension of the observed maps is  $\sim 1''$  with a pixel size depending on the beam size of the observation (see Sect. 2) resulting in typical maps size of  $\sim 15 - 20$  pixels in linear diameter. We thus generate simulated maps using a 3D disc model with radius of  $R = 20$  pixels filled by  $N_p = 5 \times 10^6$  clouds. These values turned out to be the best compromise to smooth the stochastic oscillations of the clouds numerical density and to avoid spurious numerical effects at the boundary of the model while simultaneously keeping the computational time relatively short.

The 3D disc model is then projected on the sky plane and, according to Eq. 1, the observed image of the simulated flux map depends on the normalisation constant  $I_0$ , the scale radius  $R_D$  and on the geometrical parameters: the coordinates of the map centre ( $x_0, y_0$ ), the inclination w.r.t. the sky plane ( $\beta$ ) and the position angle of the line of nodes ( $\gamma$ ) measured clockwise w.r.t. the East. Note that, for the purposes of this work, we were not interested on the physical value of  $I_0$ .



**Table 2.** The key parameters estimated from integrated spectra and kinematical modelling.

No. <sup>a</sup>	Object ID	$z_{[\text{CII}]}$ <sup>b</sup>	$R_D$ <sup>c</sup> (kpc)	$M_{\text{dyn}}$ <sup>d</sup> ( $10^{10} M_{\odot}$ )	$\sin \beta$
2	VHS J2101-5943 <sup>†</sup>	$2.307262 \pm 0.000007$	$2.95 \pm 0.11$	$2.6^{+1.5}_{-0.9}$	$0.73^{+0.17}_{-0.15}$
6	SDSS J1328-0224	$4.64616 \pm 0.00002$	$0.776 \pm 0.015$	$0.26^{+0.03}_{-0.02}$	$0.84^{+0.02}_{-0.03}$
7	SDSS J0923+0247	$4.654876 \pm 0.000015$	$0.850 \pm 0.008$	$0.6^{+1.6}_{-0.3} \times 10^1$	$0.48^{+0.18}_{-0.23}$
9	SDSS J0129-0035	$5.778883 \pm 0.000010$	$0.626 \pm 0.006$	$> 0.78 \times 10^1$	$< 0.16$
10	SDSS J1044-0125	$5.78440 \pm 0.00006$	$1.14 \pm 0.07$	$3.7^{+3.2}_{-0.3}$	$0.90^{+0.03}_{-0.26}$
11	SDSS J1306+0356	$6.03332 \pm 0.00003$	$3.21 \pm 0.09$	$1.8^{+0.9}_{-0.4}$	$0.70^{+0.08}_{-0.13}$
12	SDSS J2310+1855	$6.002841 \pm 0.000011$	$0.876 \pm 0.006$	$3.3^{+0.9}_{-0.9}$	$0.58^{+0.11}_{-0.06}$
14	SDSS J2054-0005	$6.038828 \pm 0.000009$	$0.595 \pm 0.007$	$0.7^{+4.5}_{-0.3}$	$0.64^{+0.21}_{-0.42}$
19	ULAS J1319+0950	$6.13334 \pm 0.00004$	$1.50 \pm 0.03$	$> 4 \times 10^2$	$< 0.12$
22	PSO J308-21	$6.23265 \pm 0.00004$	$0.9 \pm 0.02$	BIMODAL DISTRIBUTIONS	
25	PSO J183+05	$6.43835 \pm 0.00002$	$1.30 \pm 0.01$	$> 2 \times 10^1$	$< 0.24$
26	PSO J167-13	$6.514770 \pm 0.000015$	$4.28 \pm 0.08$	$1.69^{+0.14}_{-0.11} \times 10^1$	$0.83^{+0.03}_{-0.04}$
28	VIKING J0305-3150	$6.61434 \pm 0.00002$	$1.231 \pm 0.019$	BIMODAL DISTRIBUTIONS	

**Notes.** <sup>a</sup>Identification numbers refer to that in Table 1. <sup>b</sup>Redshift estimates obtained from the line integrated spectra. <sup>†</sup>This source is observed in CO(3-2), therefore the redshift estimate refers to this line. <sup>c</sup>Uncertainties on scale radius are statistical errors provided from  $\chi^2$ -minimization algorithm (see Sect. 4.2). <sup>d</sup>Uncertainties on dynamical masses are statistical errors computed using the posterior probability distributions of  $M_{\text{dyn}}$  ignoring any possible systematic biases: lower limits, nominal values and the upper limits correspond to 16th, 50th and 84th percentile respectively. Bimodal posterior probability distributions of the inclination angle (and dynamical mass) are explicitly indicated. In the case of bimodal distributions no values are provided and the corresponding object is rejected from the final sample.

The aforementioned parameters are free to vary during the fit procedure. Thus, to retrieve their best estimations we carried out the 2D map fit using the `cap-mpfit` PYTHON procedure part of `pPXF` package by Cappellari & Emsellem (2004) based on `minpack-1` (Moré et al. 1980) performing Levenberg-Marquardt least-squares minimisation between the data and the model. For each map, the best model minimised the following function:

$$\chi^2 = \sum_{p,p'} \left[ \frac{\tilde{F}(x_p, y_{p'}) - F(x_p, y_{p'}; [I_0, R_D, \beta, \gamma, x_0, y_0])}{\sigma_F(x_p, y_{p'})} \right]^2 + \mathcal{P}, \quad (3)$$

where  $\tilde{F}$ ,  $F$  and  $\sigma_F$  are respectively the observed flux map, flux model map and flux error map. Note that, in addition to the standard  $\chi^2$  function, we inserted in Eq. 3 a penalty term  $\mathcal{P} = 5 \times N_{\text{out}}$ , where  $N_{\text{out}}$  is the number of pixels defined in data but not in model. Indeed, the sum in Eq. 3 is computed taking into account only the pixels  $(x_p, y_{p'})$  on the observed map in which the model is defined. Hereby, unless the model is defined in all the pixels in which the observed data are present, during the minimisation process, the penalty term  $\mathcal{P}$  ensures to adequately penalise configurations for which the model cannot reproduce the data in all the points (e.g., since the disc model is thin, completely edge-on disc configuration are highly unlikely unless the PSF is large enough).

In order to obtain a robust  $\chi^2$  minimisation avoiding the convergence to a possible local minimum, the 2D flux map fit is performed multiple times by fixing the disc inclination angle ( $\beta$ ) to 5 deg up to 90 deg with a step size  $\Delta\beta = 5$  deg. For each value of  $\beta$ , the  $\chi^2$  function in Eq. 3 is minimised with respect to the free parameters  $[I_0, R_D, \gamma, x_0, y_0]$ . At the end of each step we retrieve the minimum of  $\chi^2(\beta)$  function and the corresponding set of best values of free parameters. We then use them as starting points for the next step. Once the minimisation is performed for all the inclination values in the range [5, 90] deg, we sample the curve

of minima as a function of disc inclination angle, i.e.  $\chi_m^2(\beta)$ . Finally, by finding the absolute minimum of  $\chi_m^2(\beta)$ , we retrieve the best set of  $[I_0, R_D, \beta, \gamma, x_0, y_0]$ . Following the method illustrated above we estimated the best value of  $R_D$  measured in arcseconds for all the 18 objects indicated in Table 1 with flag [rot]="r". Finally, we compute  $R_D$  values in physical length, using the redshift estimates obtained in Sect. 3.1.

In the next section we use the  $R_D$  estimates to compute the kinematical model in order to perform the 2D fit of the velocity fields. For this purpose, we use the  $\chi_m^2(\beta)$  curve as a *prior* knowledge on disc inclination angle. As an example, in Fig. 7 we show flux map modelling results and the correspondent  $\chi_m^2(\beta)$  curve for SDSS J0923+0247. The  $R_D$  values are listed in Table 2 for those objects with constraint on dynamical mass (see also Appendix E).

#### 4.3. Estimation of $M_{\text{dyn}}$ : 2D fit of the velocity maps

In order to estimate the dynamical masses of the quasars sample, we performed the 2D fit of LOS velocity maps. At high- $z$ , uncertainties on the dynamical mass estimates are mainly driven by the poor angular resolution of observations. As the integrated flux map of line emission, even the velocity maps are affected by beam smearing thus introducing additional uncertainties in the fitting parameters (as also pointed out by other authors, see e.g., Bosma 1978; Begeman 1987; de Blok & McGaugh 1997; O'Brien et al. 2010; Swaters et al. 2000; Epinat et al. 2009, 2010; Swaters et al. 2009; Carniani et al. 2013; Kamphuis et al. 2015). This effect is such that disc inclination angle and dynamical mass become almost degenerate parameters, i.e. the observed velocity field can be similarly reproduced by different couple  $(\beta, M_{\text{dyn}})$  with similar  $M_{\text{dyn}} \sin^2 \beta$ , thus providing very near values of  $\chi^2$  function (see also e.g., Epinat et al. 2010). In Fig. 6 we show the effect of the beam smearing on the iso-velocity curves of simulated velocity fields.

Consistently with the method illustrated in Sect. 4.1, we perform fits of velocity maps using thin rotating disc models defined by exponential mass distributions with  $R_D$  values estimated in Sect. 4.2. In order to retrieve the best-fitting model and to estimate the parameter uncertainties, we used the PYTHON Affine Invariant Markov chain Monte Carlo (MCMC) Ensemble sampler `emcee` (Foreman-Mackey et al. 2013). For this purpose we defined the likelihood function of a model given the data as:

$$\begin{aligned} \ln p = & -\frac{1}{2} \left( \frac{\bar{x}_0 - x_0}{\Delta x_0} \right)^2 - \frac{1}{2} \left( \frac{\bar{y}_0 - y_0}{\Delta y_0} \right)^2 + \\ & - \frac{1}{2} \sum_{p,p'} \left\{ \frac{[\tilde{V}(x_p, y_{p'}) - V(x_p, y_{p'}; [\mu, \gamma, \sin \beta, x_0, y_0]) - V_{\text{sys}}]^2}{\sigma_V^2(x_p, y_{p'})} \right\} + \\ & + \ln \left[ 2\pi (\sigma_V^2(x_p, y_{p'})) \right] \Bigg\} - \frac{1}{2} \mathcal{P}, \end{aligned} \quad (4)$$

where  $\tilde{V}$ ,  $V$  and  $\sigma_V$  are the observed velocity map, simulated velocity map and velocity errors map, respectively.

The simulated field depends on geometrical parameters, the scale radius and the dynamical mass (see Eq. 2). However, instead of  $M_{\text{dyn}}$  we used  $\mu = \log(M_{\text{dyn}} \sin^2 \beta)$  as free parameter, since it is decoupled from disc inclination thus uniquely determines the intrinsic velocity field. Here, we also take into account the systemic velocity of the galaxy, i.e.  $V_{\text{sys}}$ , as additional free parameter. Furthermore, defining the likelihood function in Eq. 4 we assume Gaussian priors for the coordinates of the galaxy centre with maximum probability corresponding to  $(x_0, y_0)$  obtained from the flux map modelling as illustrated in Sect. 4.2. Here,  $\Delta x_0$  and  $\Delta y_0$  are the standard deviations assumed equal to 0.1 pixel. In addition, we assume box-like prior on the position angle of the disc ( $-180 \leq \gamma(\text{deg}) \leq 180$ ) and on the dynamical mass ( $M_{\text{dyn}} > 0$ ). Finally, we account for prior knowledge on disc inclination from morphology by imposing that, during the fitting process,  $\Delta \chi_m^2(\beta) < \max\{\Delta \chi_m^2(\beta)\}/2$ ; where  $\Delta \chi_m^2(\beta) = \chi_m^2(\beta) - \chi_M^2$  with  $\chi_M^2$  the absolute minimum of  $\chi_m^2(\beta)$  curve resulting from the fit of flux map (see Sect. 4.2).

We thus maximise the Eq. 4 using  $[V_{\text{sys}}, \mu, \gamma, \sin \beta, x_0, y_0]$  as free parameters and we recover their *posterior* probability distributions<sup>2</sup>. Finally, the best values of parameters and related uncertainties are estimated by computing the 16th, 50th and 84th percentile of the distributions. As an example, Fig. 7 shows the kinematical modelling of SDSS J0923+0247 (see also Appendix E).

Due to the poor spatial resolution of some observations we have successfully constrained the disc inclination and the dynamical mass for only 13 objects of the sample (see Table 2). We note that for two of them we find bimodal distributions for  $\sin \beta$  and  $\mu$ , thus not allowing to define unique values.

## 5. Determination of the black hole masses

Currently, the only possible technique to carry out black hole mass estimates at high- $z$  is by using Single Epoch (SE) virial relation that combines the FWHM or the line emission originated in the broad line region (BLR) of quasar, with the continuum luminosity emitted from the BH accretion disc (e.g., McLure & Dunlop 2004; Vestergaard & Peterson 2006; Vestergaard & Osmer 2009; but see also e.g. Trevese et al. 2014; Grier et al. 2019). This approach assumes that the BLR is virialised and that there

is a tight relation between the BLR radius ( $R_{\text{BLR}}$ ) and the continuum luminosity of the AGN ( $L_{\text{AGN}}$ ) (e.g., Kaspi et al. 2005; Bentz et al. 2006, 2009). Under these assumptions,  $L_{\text{AGN}}$  and the FWHM of the broad emission lines are used as proxy for  $R_{\text{BLR}}$  and virial velocity, respectively.

To date, thanks to the effort of various groups (e.g., McLure & Jarvis 2002; McLure & Dunlop 2004; McGill et al. 2008; Wang et al. 2009; Shen et al. 2011; Denney 2012; Park et al. 2013; Coatman et al. 2017), many relations have been calibrated employing different broad lines in order to infer the  $M_{\text{BH}}$  by assuming that such BH mass estimates are in agreement with reverberation mapping BH masses (Vestergaard & Peterson 2006) which, in turn, are in agreement with local BH-galaxy scaling relations for normal galaxies (Onken et al. 2004). This is motivated by the unknown geometry and kinematics of the BLR (e.g., McLure & Dunlop 2001; Onken et al. 2004). In high-redshift quasars, the atomic transitions of MgII and CIV are the most common and brightest BLR lines that are observed in optical (rest-frame UV) spectra, and thus they are extensively used as virial mass estimator with the corresponding continuum luminosity measured by convention at 3000Å and 1550Å for MgII and CIV respectively. However, the reliability of CIV line is still strongly debated. Firstly, the CIV scaling relation is based of very few measurements (Kaspi et al. 2007; Saturni et al. 2016; Park et al. 2017); secondly CIV line is often associated with broad and blueshifted wings likely due to outflows (e.g., Richards et al. 2011; Denney 2012) that may affect the measure of the line width biasing the BH mass estimates. We note that the aforementioned calibrations have intrinsic uncertainties of the order of  $\sim 0.3 - 0.4$  dex (see, e.g. Vestergaard & Peterson 2006; Denney 2012; Park et al. 2017) that are usually larger than the errors associated to line width and flux measurements.

### 5.1. Black hole masses from the literature

In this work we adopted a unique SE virial relation to estimate the BH masses of our sample in a homogeneous way. In details, we use the relation by Bongiorno et al. (2014), which has been calibrated by assuming the BH-galaxy scaling relations by Sani et al. (2011). This latter is consistent with the relation used as a  $z = 0$  reference for studying the redshift evolution (i.e. e.g., Kormendy & Ho 2013; de Nicola et al. 2019):

$$\begin{aligned} \log \left( \frac{M_{\text{BH}}}{M_{\odot}} \right) = & 6.6 + 2 \log \left( \frac{\text{FWHM}(\text{MgII})}{10^3 \text{ km s}^{-1}} \right) + \\ & + 0.5 \log \left( \frac{\lambda L_{\lambda}(3000\text{\AA})}{10^{44} \text{ erg s}^{-1}} \right). \end{aligned} \quad (5)$$

Thus, where available, we retrieved MgII FWHM and the continuum luminosity estimates from the literature and, if not available, we assumed  $M_{\text{BH}}$  estimates provided in the literature.

Summarising, we recover BH masses from the literature for all but PSO J308-21 and PSO J183+05, using H $\beta$ , MgII and CIV BLR lines. For SDSS J0129-0035 and SDSS J2054-0005 the black hole masses are estimate from the bolometric luminosity ( $L_{\text{bol}}$ ) assuming Eddington accretion ( $L_{\text{bol}}/L_{\text{Edd}} = 1$ ). We note that this assumption is supported by some evidences showing that black holes at  $z \gtrsim 6$  accrete matter with a rate comparable to the Eddington limit (De Rosa et al. 2014; Mazzucchelli et al. 2017). The data are listed in Table 3. The BH masses computed in this work by using Bongiorno et al. (2014) calibrations are a factor  $\sim 2$  smaller than those reported in literature using different calibrations (see references in Table 3 for full details).

<sup>2</sup> We set up the MCMC procedure with 50 walkers performing 1000 step each for a total of  $5 \times 10^4$  evaluations of the log-likelihood function.

**Table 3.** Black hole masses retrieved from literature and spectroscopic data used to estimate  $M_{\text{BH}}$  through MgII-based virial relation.

No. <sup>a</sup>	Object ID	FWHM(MgII) (km s <sup>-1</sup> )	$\lambda L_{\lambda}(3000\text{\AA})$ (10 <sup>46</sup> erg s <sup>-1</sup> )	$M_{\text{BH}}^b$ (M <sub>⊙</sub> )	References <sup>c</sup>
2	VHS J2101-5943	-	-	$3.2 \pm 0.7 \times 10^{10}$	Ban2015
6	SDSS J1328-0224	$3815 \pm 954$	$1.9 \pm 0.4$	$8 \pm 4 \times 10^8$	Tra2011
7	SDSS J0923+0247	$2636 \pm 264$	$1.4 \pm 0.3$	$3.3 \pm 1.0 \times 10^8$	Tra2011
9	SDSS J0129-0035	-	-	$1.7^{+3.1}_{-1.1} \times 10^8$	Wan2013
10	SDSS J1044-0125	-	-	$5.6 \pm 0.5 \times 10^9$	She2019
11	SDSS J1306+0356	$3158 \pm 145$	$2.45 \pm 0.06$	$6.3 \pm 1.5 \times 10^8$	DeR2011
12	SDSS J2310+1855	$4497 \pm 352$	$6.027 \pm 0.018$	$2.0 \pm 0.6 \times 10^9$	She2019
14	SDSS J2054-0005	-	-	$0.9^{+1.6}_{-0.6} \times 10^9$	Wan2013
19	ULAS J1319+0950	$3675 \pm 17$	$3.8 \pm 1.0$	$1.1 \pm 0.2 \times 10^9$	Sha2017
26	PSO J167-13	$2350 \pm 470$	$1.5 \pm 0.7$	$2.7 \pm 1.4 \times 10^8$	Ven2015
28	VIKING J0305-3150	$3189 \pm 85$	$1.66 \pm 0.02$	$5.2 \pm 1.2 \times 10^8$	DeR2014

**Notes.** <sup>a</sup>Identification numbers (No.) refer to that in Table 1. <sup>b</sup>Black hole mass estimated using Single Epoch virial relation in Eq. 5 when possible, otherwise the value provided here is the one available in literature (see references for full details). The uncertainties we report do not include the systematic uncertainties intrinsic to the  $M_{\text{BH}}$  estimators. <sup>c</sup>References: Ban2015 - Banerji et al. (2015); DeR2011, DeR2014 - De Rosa et al. (2011, 2014); Sha2017 - Shao et al. (2017); She2019 - Shen et al. (2019); Tra2011 - Trakhtenbrot et al. (2011); Ven2015 - Venemans et al. (2015); Wan2013 - Wang et al. (2013)

However both estimates are consistent within the typical uncertainties ( $\sim 0.4$  dex).

## 5.2. Black hole mass from LBT data

The study of the redshift evolution of  $M_{\text{BH}} - M_{\text{dyn}}$  relation can be severely affected by reliability of  $M_{\text{BH}}$  estimates; in particular, the available spectroscopic information for our sample did not allow us to derive  $M_{\text{BH}}$  measurements with a unique method.

We therefore started an observational campaign at LBT (Large Binocular Telescope) of the sources which  $M_{\text{BH}}$  estimates were derived assuming  $L_{\text{bol}}/L_{\text{Edd}} = 1$  (SDSS J0129-0035, SDSS J2054-0005 and SDSS J2310+1855), and of two additional targets without previous  $M_{\text{BH}}$  estimates from the literature (PSO J308-21 and PSO J138+05; even though dynamical masses of these two sources are tentative). We thus obtain NIR spectra of the quasars with LUCI (LBT Utility Camera in the Infrared) targeting the CIV line and the adjacent continuum which are redshifted into the  $zJ$  filter (central  $\lambda = 1.17 \mu\text{m}$ ), for all but PSO J183+05. In fact, for all these sources the MgII line falls in a spectral region with a very low atmospheric transmission. For PSO J183+05, instead, we targeted the BLR MgII line, which is redshifted at  $\approx 2.0817 \mu\text{m}$  and can be observed with the  $HK$  filter (central  $\lambda = 1.93 \mu\text{m}$ ).

Unfortunately we did not achieve the requested sensitivities due to bad weather conditions. No BLR emission lines have been detected in all quasars but J2310+1855, for which we derived a CIV-based  $M_{\text{BH}}$  estimate of  $6 \times 10^9 M_{\odot}$  (see Appendix D for full details of the observations). Our estimation is consistent, within the error, with that reported by Feruglio et al. (2018) and Shen et al. (2019). We note that Shen et al. (2019), who published NIR spectra of a large sample of  $z \sim 5.7$  QSOs, also provide a  $M_{\text{BH}}$  measurement for J2310+1855 through virial relation based on MgII as well. In the following we will refer to the MgII estimate from Shen et al. (2019), because of the aforementioned issues related to CIV-based measurements.

## 6. Summary of sample sub-selections

The data analysis described in Sects. 3 and 4 has been performed on the 32 continuum-subtracted cubes of the sources listed in Table 1. Each step of the analysis has led to the rejection of a number of objects which turned out not to be suitable for the method adopted in this work. Here we briefly summarise the different sub-selections occurred throughout this work:

1. By inspecting the velocity maps and red/blue residuals maps (see Sect. 3.3 for details), 14 objects ( $\sim 45\%$ , flagged with [rot]="u" in Table 1) do not show spatially resolved kinematics or rotating disc kinematics. This is possibly due to the presence of outflows or merging events or of a companion located in the proximity (projected on the sky plane) of the quasar. For this purpose, velocity dispersion maps provide additional information on the kinematics. However, in the case of the rejected sources, a comprehensive interpretation of the observed complex velocity fields is beyond the scope of this work. However, excluding these objects from the final sample could bias the results (see Sect. 7.4). As the result of this analysis the sample has been reduced to 18 objects.
2. We then performed the fits of the flux and velocity maps (see Sect. 4.2 and 4.3 for details) on the remaining 18 objects selected in the previous step. As a result, for 5 objects ( $\sim 30\%$ ) the kinematical modelling has not enabled us to constrain the disc inclination, i.e., the dynamical mass. Possibly, wrong assumptions on the mass distribution (see Eq. 1) and/or the poor angular resolution of the observations making inclination and dynamical mass almost degenerate parameters (see Sect. 4.3) have prevented the determination of the mass in these host galaxies. In addition, the iso-velocity curves of the kinematical fields are typically distorted suggesting the presence of non-circular motion. In particular for 2 objects (PSO J308-21, VIKING J0305-3150) the posterior probability distributions of the inclination angle  $\beta$  (and  $\mu$ ) are bimodal, preventing us to constrain these parameters. For 3 objects (PSO J183+05, SDSS J0129-0035, ULAS J1319+0950) we derived an upper limit on the disc inclination, i.e. a lower limit on mass  $M_{\text{dyn}}$ . Summarising, we obtained 8 constrained, 2



bimodal and 3 lower limit measurements of the dynamical mass (see Table 2).

3. The final step is to relate our dynamical mass estimates with  $M_{\text{BH}}$  retrieved from the literature. We illustrate this step in Sect. 5 and 8. Despite several studies performed in this field aiming to estimate  $M_{\text{BH}}$  even for high redshift quasars, for 2 objects ( $\sim 15\%$  of the remaining 13 resulted from the previous step) black hole mass estimates were not available at the time this paper was written. Therefore, we rejected these objects out from the final sample (see Table 3). These quasars are flagged with  $[M_{\text{BH}}] = \text{"u"}$  in the Table 1.

These selection steps are shown in the scheme drawn in Fig. 8.

## 7. Comparison of results and uncertainties on dynamical mass estimates

In Sect. 7.1 we compare our results with those obtained by other authors who attempted to perform a full kinematical modelling of individual sources which belong to our sample.

Other works highlighted the presence of companion sources in the close environment of a few QSOs analysed in this work. Such satellites galaxies can disturb the gas kinematics of the host through tidal interaction thus introducing additional uncertainties in measuring the galaxy dynamical mass. We discuss this point in Sect. 7.2.

In Sect. 7.3 we discuss the limit of validity of the assumption of rotating disc model and the possible mass contribution arising from random motions throughout the galaxy (see also Appendix B).

Finally, in Sect. 7.4, we investigate observational biases possibly arising from the sub-selection of the sample.

### 7.1. Comparison of results from other kinematical modelling in the literature

#### 7.1.1. ULAS J1319+0950

Jones et al. (2017) and Shao et al. (2017) performed a kinematical characterisation of [CII] emission of J1319+0950 by using a tilted rings warp-less model and assuming purely circular rotation. They inferred respectively a dynamical mass of  $15.8 \times 10^{10} M_{\odot}$  and  $13.4 \times 10^{10} M_{\odot}$  and inclination angle of 29 deg and 33 deg, which are roughly consistent with the value estimated by Wang et al. (2013) by using the axial ratio of the [CII] flux map to estimate the disc inclination and the [CII] FWHM as estimate of maximum circular velocity. Furthermore, by fitting the dust continuum emission in  $uv$  plane, Carniani et al. (2019) inferred an inclination angle of  $\sim 15$  deg. In contrast we are not able to constrain disc inclination angle from our kinematical modelling resulting in a lower limit on dynamical mass ( $> 4 \times 10^{12} M_{\odot}$ ). The disagreement between our result and the previous ones may arise from the beam smearing effect that is not taken into account in the model used by Jones et al. (2017) and Shao et al. (2017). As discussed in Sect. 4.3 beam smearing strongly affects the observed velocity gradients and introduces additional uncertainties in the fitting parameters. In addition, Shao et al. (2017) mentioned that current data cannot fully rule out the presence of a bidirectional outflow which introduce additional uncertainty of the dynamical mass. In such case, the strong deviation of the ratio  $M_{\text{BH}}/M_{\text{dyn}}$  could be associate to a wrong kinematical modelling of the observed data for which we also assume rotating disc kinematics as in Jones et al. (2017) and Shao et al. (2017).

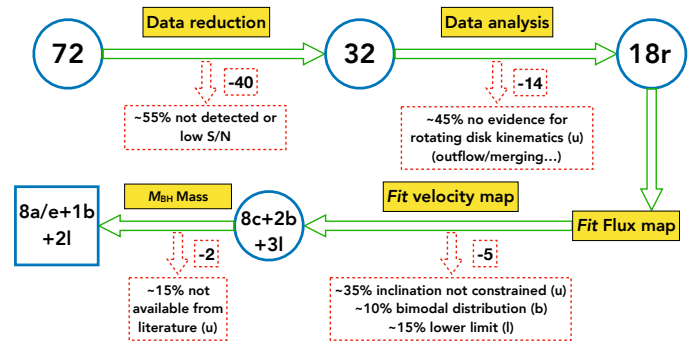


**Fig. 8.** The scheme summarise the different sub-selections occurred throughout this work. Starting from an initial sample of 72 quasar host galaxies observations extracted from the ALMA data archive, the final sample is composed by 10 high- $z$  objects for which we study the BH-galaxy relation. The characters indicating the selection type are in accordance with Table 1. The number of objects rejected out from the sample is also indicated at each step.

#### 7.1.2. VIKING J0305-3150

High angular resolution ( $0.076'' \times 0.071''$ ) ALMA [CII] observations of J0305-3150 has been recently presented and analysed by Venemans et al. (2019). The resulting analysis highlights that the distribution and kinematics, as traced by the [CII] emission, are highly complex with the presence of cavities and blobs.

Venemans et al. (2019) attempted to modelling the kinematics adopting different 3D models (thin rotating disc with constant velocity, Keplerian disc, truncated disc and simple AGN model embedded in a uniform rotating spherical gas) taking into account beam smearing effects and the pixels correlation within the beam with a bayesian approach. The results show that the gas kinematics in J0305-3150 appears to be dispersion-dominated with some overall rotation in the central kiloparsecs and cannot easily reproduced by a simple rotating disc model with the implication that most of the gas has not settled in a disc yet. In addition, authors point out that energy injection into the ISM produced by AGN feedback processes and the presence of a companion in the close environment may be play an important role in producing the observed [CII] cavities and in perturbing the gas kinematics.

In conclusion a simple model of rotating disc is not sufficient to match the [CII] observations of J0305-3150 also derived by our analysis, where  $M_{\text{dyn}}$  is unconstrained by the simple model assumed.

#### 7.1.3. SDSS J1044-0125 & SDSS J0129-0035

In the work by Wang et al. (2019) authors carried out observation of J1044-0125 and J0129-0035 through the ALMA program 2012.1.00240.S (the same dataset used in this work for the latter source) with angular resolution of  $\sim 0.2''$ . The authors show that gas in J1044-0125, as traced by [CII] emission, does not show a clear sign of rotation suggesting very turbulent gas velocity field. Furthermore, [CII] spectrum reveals offset components that could be associated with a node of outflowing gas or the dense core of a satellite galaxy that contribute to increase the dispersion velocity component of the gas in the host galaxy. On the other hand, the lower angular resolution data used in this work ( $\sim 0.6'' \times 0.5''$ , ALMA program 2011.0.00206.S, see Wang et al. 2013) reveal the presence of a velocity gradient. This could be the results of beam smearing effects producing a smoothing of the rapid changing velocity gradients. In the case of J1044-

0125, we find that the observed velocity field is roughly consistent with a nearly edge-on rotating disc model. Therefore, we conclude that our dynamical mass estimate is tentative. We also note that, Wang et al. (2019) show that [CII] and dust emission in the nuclear region of J1044-0125 and J0129-0035 follow an exponential light profile, in accordance with the hypothesis underlying our model.

In the case of J0129-0035, the observations analysed in Wang et al. (2019) reveal that [CII]-emitting gas shows clear velocity gradients likely associated with a rotating disc with additional gas clumps thus suggesting complex kinematics in the nuclear region. They attempted to constrain the host galaxy dynamics adopting the same method as in Jones et al. (2017) and Shao et al. (2017) works. The results show that the kinematics is consistent with a nearly face-on rotating disc with an inclination angle of  $\beta = (16 \pm 20)$  deg and a lower limit on the dynamical mass equal to  $M_{\text{dyn}} = 2.6 \times 10^{10} M_{\odot}$ . The results are consistent with what we found in this work. BH mass of J0129-0035 is estimated as in Wang et al. (2013) assuming Eddington accretion and is the same that we used in this work. Hence, Wang et al. (2019) estimate a SMBH to host galaxy dynamical mass ratio of  $M_{\text{BH}}/M_{\text{dyn}} = 0.0066$  to be compared with  $M_{\text{BH}}/M_{\text{dyn}} = 0.0022$  that is roughly consistent with the local ratio predicted in Decarli et al. (2010) unlike the most luminous quasars with massive BHs ( $10^9 - 10^{10} M_{\odot}$ ) at this redshift that show ratios a few to  $\geq 10$  times higher (Venemans et al. 2016; Decarli et al. 2018). Therefore, as pointed out by Wang et al. (2019), this results may suggest that the BH-galaxy coevolution of less massive system ( $M_{\text{BH}} \sim 10^7 - 10^8 M_{\odot}$ ) in the early universe are evolving more closer to the trend of local galaxies (see also, Willott et al. 2010, 2015b, 2017; Izumi et al. 2018, 2019).

## 7.2. Possible contamination due to the presence of companion sources in the quasar close environment

Decarli et al. (2017) serendipitously discovered companion galaxies in the same ALMA field of SDSS J0842+1218, CFHQS J2100-1715, PSO J231-20 and PSO J308-21. Such companions appear similar to the host galaxies of quasars in terms of [CII] brightness and implied dynamical mass, but do not show evidence of AGN activity. The analysis led in this work on the same dataset used in Decarli et al. (2017) (ALMA program 2015.1.01115.S), show that the kinematics is unresolved (flag [rot]="u"; see Table 1) in the case of J0842+1218 and J2100-1715 (beam size of  $\sim 1.0'' \times 0.9''$  and  $\sim 0.7'' \times 0.6''$  respectively); and marginally resolved (disc inclination angle is unconstrained; flag [ $\beta$ ]="u"; see Table 1) in the case of J231-20 (beam size of  $\sim 1.0'' \times 0.8''$ ). This last source together with J308-21 have a [CII]-bright companion at small projected separation of  $\sim 10$  kpc suggesting a strong gravitational interaction between quasar and companion able to alter the disc kinematics increasing the velocity dispersion component of the gas. In particular Decarli et al. (2017) show that the [CII] emission of J308-21 stretches over about  $4''$  ( $\approx 25$  kpc) and more than  $1000 \text{ km s}^{-1}$  connecting the companion source suggesting that is undergoing a tidal disruption due to the interaction or merger with the quasar host. This scenario is successively supported by higher angular resolution ( $\sim 0.3''$ ; ALMA program 2016.A.00018.S) follow-up observation of J308-21 presented in Decarli et al. (2019); the same dataset used in this work. However, the bulk of [CII] emission of the quasar host galaxy show a spatially resolved velocity gradient that in our work we attempt to model with a rotating disc by excluding pixels that are clearly not associated with the quasar host. Nevertheless, our analysis leads to a bimodal pos-

terior probability distribution of disc inclination angle and dynamical mass parameters of J308-21. We can thus conclude that the complex kinematics of this system highlighted in the previous analysis presented in Decarli et al. (2017, 2019), cannot be easily interpreted with a simple rotating disc likely due to the perturbed kinematics caused by the strong interaction with the satellite galaxy.

Willott et al. (2017) analyse the source PSO J167-13 observed in ALMA Cycle 3 project 2015.1.00606.S; the same dataset analysed in this work. This source shows an asymmetric continuum emission that is more extended to the south-east than north-west of the peak. This excess is located at  $\approx 0.9''$  (projected distance  $\approx 5.0$  kpc) and it is associated with a companion galaxy whose [CII] blueshifted ( $270 \text{ km s}^{-1}$ ) emission corresponds to about 20% of the QSO [CII] luminosity. The P-V diagram of the source shows a positive velocity gradient, suggesting a rotating disc geometry. With this assumption Willott et al. (2017) infer the dynamical mass of  $M_{\text{dyn}} = 2.3 \times 10^{11} M_{\odot}$  using the axial ratio of the quasar (excluding the companion source) [CII] flux map as an estimate of the disc inclination angle. The black hole mass of J167-13,  $M_{\text{BH}} = (4.0 \pm 2.0) \times 10^8 M_{\odot}$ , is estimated in Venemans et al. (2015) by using calibration based on MgII broad emission line (Vestergaard & Osmer 2009). By comparison, we measure a dynamical mass of  $1.67^{+0.14}_{-0.11} \times 10^{11} M_{\odot}$  and a black hole mass of  $M_{\text{BH}} = (2.7 \pm 1.4) \times 10^8 M_{\odot}$  (see, Sect. 5 for details) resulting in a ratio of  $M_{\text{BH}}/M_{\text{dyn}} = 0.0016$  that is completely consistent with the value found by Willott et al. (2017) ( $M_{\text{BH}}/M_{\text{dyn}} = 0.0017$ ) and with the prediction of the local relation (Decarli et al. 2010; Kormendy & Ho 2013).

Neeleman et al. (2019) further investigate the aforementioned four quasar host – companion galaxy pairs of J0842+1218, J2100-1715, J231-20, J167-13 by analysing high angular resolution ( $\sim 0.4'' \times 0.3''$ ) ALMA observations of [CII] emission. They observe tidal interactions disturbing the gas in these high- $z$  galaxies making the ISM turbulent thus confirming previous results of Decarli et al. (2018, 2019) and Willott et al. (2017). Furthermore, these high angular resolution observations reveals that [CII] emission of SDSS J1306+0356 arises from two spatially and spectrally distinct sources with a physical separation of  $5.4$  kpc that are tidally interacting. Neeleman et al. (2019) model the [CII] kinematics of the galaxies pairs with a rotating thin disc model taking into account the beam smearing and the correlation between pixels. They found upper limit on dynamical masses for all but J167-13 and J2100-1715. In particular they measure a dynamical mass of  $(3.5 \pm 0.4) \times 10^{10} M_{\odot}$  for the J167-13 quasar. This value is about one order of magnitude lower compared to the result of Willott et al. (2017) and our work. In our estimate we take into account also the emission from the companion galaxy thus possibly overestimating the quantities derived from the total integrated spectrum (FWHM<sub>[CII]</sub>, [CII] flux, luminosity, etc., see Table A.1 in Appendix A), the scale radius of the mass profile and the total mass content of the quasar host galaxy. This could explain the inconsistency on the our dynamical mass measurements of J167-13 compared to the Willott et al. (2017) and Neeleman et al. (2019) works.

## 7.3. Limit on the assumption of thin rotating disc

The comparison of our results discussed in Sect. 7.1 and 7.2, has highlighted that, at least in some cases, the assumption of a thin rotating disc is too simplified to properly describe the observed complex kinematic field. Furthermore, from the analysis of the velocity maps, we find extreme cases in which the

disc inclination w.r.t. the sky plane is very low (e.g., ULAS J1319+0950), compatible with a face-on configuration. However, for these objects, the observed velocity dispersion are still high ( $\sim 100\text{--}200\text{ km s}^{-1}$ , as visible in the figures in Appendix E), which is not expected for a thin face-on discs.

The observed velocity dispersion, can be produced both by instrumental effect and random motions throughout the galaxy (see e.g., Flores et al. 2006; Weiner et al. 2006; Epinat et al. 2010). Different authors (e.g., Cresci et al. 2009; Epinat et al. 2009; Taylor et al. 2010) point out that random motions can support part of the mass. In this case, by modelling the kinematics with a rotating disc could result in underestimating the galaxy dynamical mass. In Appendix B, we investigate the contribution of random motions to the dynamical mass and find that in our sample the mass supported by non-rotational motions is negligible, i.e., it is included within the dynamical mass uncertainties. Therefore we conclude that the rotating gas disk model provide an overall good description for the gas kinematics of our QSO host galaxies.

#### 7.4. Potential observational biases in excluding the unresolved objects

In Sect. 3.3, we investigate whether the observed kinematics are spatially resolved. Out to 32 objects with a line detection, 14 ( $\geq 40\%$ ) are rejected from the final sample (see also Sect. 6). Excluding those objects that are spatially unresolved could result in an observational bias. In fact, if these sources are significantly less massive than the others might therefore bias the results to more massive host galaxies.

The observed size of the line emitting region may depend on both the achieved sensitivity and the angular resolution. Therefore, in the case of spatially unresolved emission, it is difficult to asses if this is due to the intrinsic compact size of the galaxy or to the low sensitivity level of the observations. For this purpose, deeper observations of these objects with similar observational setups could help in order to make a fair comparison of the observed size. However, we do not observe a strong correlation between the spatial size of the FIR line emission and the dynamical mass of the galaxy (see Table 2). Therefore, we conclude that we cannot safely argue that a possible bias is introduced in rejecting the spatially unresolved objects.

### 8. The $M_{\text{BH}} - M_{\text{dyn}}$ relation at high redshift

In order to trace the relation between black hole mass and dynamical mass for the final high- $z$  QSOs sample, we compare the  $M_{\text{dyn}}$  measurements obtained through kinematical modelling illustrated in Sect. 4 (see Table 2), with the black hole masses obtained from literature as we explained in Sect. 5 (see Table 3). The relation is shown in the plot of Fig. 9. We also report two reference relations obtained with samples of local quiescent galaxies (Kormendy & Ho 2013; de Nicola et al. 2019) and AGN (Reines & Volonteri 2015). In order to infer the average redshift evolution of the  $M_{\text{BH}} - M_{\text{dyn}}$  we adopt the relation  $\log M_{\text{BH}} = \alpha + \beta(\log M_{\text{dyn}} - 10.8)$  and we perform the fit assuming fixed slope  $\beta = 1.01 \pm 0.07$  as found by de Nicola et al. (2019), and the normalisation  $\alpha$  as the only free parameter. Furthermore, to reduce the impact of any possible outliers we execute the fit adopting *bootstrap* method on the standard  $\chi^2$  minimisation.

Using  $10^4$  bootstrap iterations we obtained the best value of  $\alpha$  and its uncertainties by computing the 16th, 50th and 84th

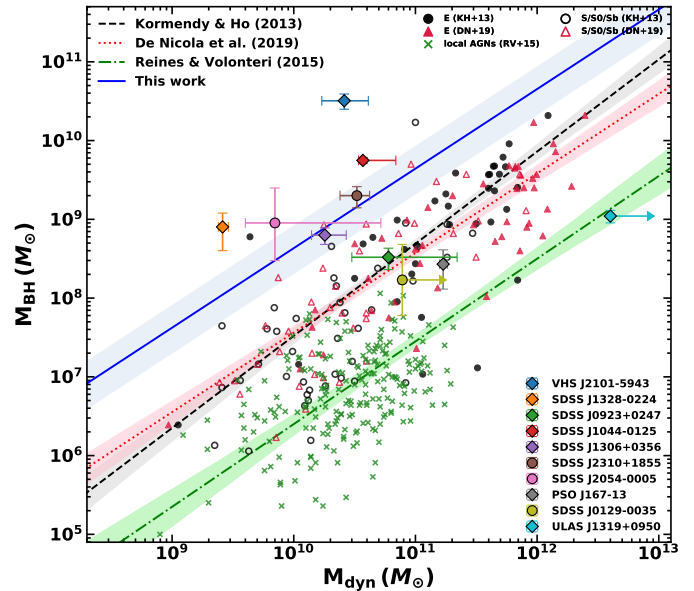


**Fig. 9.** The high redshift relation between the black hole mass ( $M_{\text{BH}}$ ) and the dynamical mass of the host galaxy ( $M_{\text{dyn}}$ ). The dashed black line and the dotted red line represent the reference local relation inferred using samples of local galaxies (E=ellipticals, S/S0/Sb=spirals) shown as black dots (Kormendy & Ho 2013, also indicated as KH+13) and red triangles (de Nicola et al. 2019, or DN+19). The green line is the relation found by Reines & Volonteri (2015, or RV+15) by measuring the total stellar mass in sample of local AGN (green crosses). The solid blue line is the best fit to our data. The shadowed areas show the  $1\sigma$  uncertainty. In the case of SDSS J0129-0035 and ULAS J1319+0950 we inferred a lower limit on the dynamical mass. We do not take into account these data in the fit. The circles of our data points indicate those sources which BH masses are estimated from bolometric luminosity assuming Eddington accretion.

percentile respectively:

$$\alpha = 9.4 \pm 0.3 \quad (6)$$

Our result is in agreement with those reported by other high- $z$  works (e.g., Decarli et al. 2010, 2018; Trakhtenbrot et al. 2015, 2017; Venemans et al. 2016, 2017b) suggesting that  $M_{\text{BH}} - M_{\text{dyn}}$  relation evolves with redshift. It should be noted that local reference relation (e.g., Kormendy & Ho 2013; de Nicola et al. 2019) is obtained using bulge stellar mass in spiral and elliptical galaxies (where, in the latter case, bulge stellar mass corresponds to the total stellar mass). As a result, the galaxy dynamical masses estimated in this work should be treated as an upper limit of the total stellar mass. By comparing our results with the relation by Reines & Volonteri (2015), who adopt the total stellar mass of the AGN host galaxy (green line in Fig. 9), we find an even stronger evolution with redshift.

#### 8.1. The evolution of $M_{\text{BH}}/M_{\text{dyn}}$ across the cosmic time

The evolution of the ratio  $\Gamma = M_{\text{BH}}/M_{\text{dyn}}$  as a function of redshift provides key information about the relative time scale between black hole growth and galaxy mass assembly. For this purpose we show the  $M_{\text{BH}}/M_{\text{dyn}}$  ratios as a function of  $z$  estimates obtained from the integrated spectra of the lines provided in Table 2. The final result is shown in Fig. 10 on which we also overplot the relation found by Decarli et al. (2010) using galaxy stellar masses of a sample of quasars at  $z \lesssim 3$ , extrapolated up



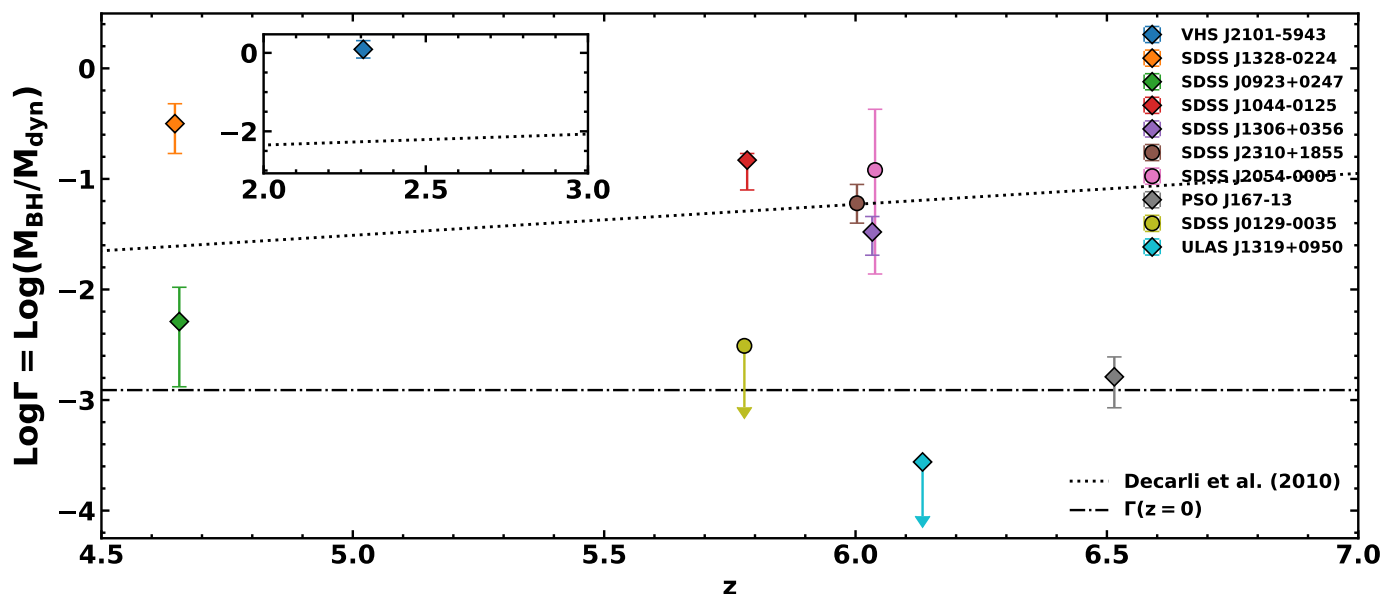


**Fig. 10.** The evolution of  $\Gamma = M_{\text{BH}}/M_{\text{dyn}}$  as a function of redshift  $z$ . The black dotted and dash-dotted lines represent respectively the relation found by Decarli et al. (2010) at  $z \lesssim 3$  and the corresponding ratio at  $z = 0$ . The inset panel shows the same plot at  $2 < z < 3$ . In the case of SDSS J0129-0035 and ULAS J1319+0950 we inferred lower limits on dynamical masses, i.e. an upper limit on the ratio  $\Gamma$ . The circles indicate those sources which BH masses are estimated from bolometric luminosity assuming Eddington accretion.

to  $z = 7$ :

$$\log \Gamma(z) = (0.28 \pm 0.06)z - (2.91 \pm 0.06). \quad (7)$$

We conclude that the trend of  $\Gamma$  that we inferred at high redshift is roughly consistent with that of Eq. 7 and thus this result confirms the evidence that  $M_{\text{BH}} - M_{\text{dyn}}$  appears to evolve with the redshift as has been highlighted in previous works (Walter et al. 2004; Decarli et al. 2010, 2018; Merloni et al. 2010; Venemans et al. 2012, 2017b).

The ratio  $\Gamma$  appear to be  $\sim 10\times$  the local value  $\log \Gamma(z = 0) = 0.28$  at  $z \sim 4 - 6$ . However, from Fig. 10 we can infer that for SDSS J0923+0247, SDSS J0129-0035, ULAS J1319+0950 and PSO J167-13 at redshift  $4.6 \lesssim z \lesssim 6.6$  the  $M_{\text{BH}}/M_{\text{dyn}}$  is consistent with the value observed for galaxies in the local Universe. Although very preliminary result, this possibly suggests a decreasing of  $\Gamma$  at  $z \gtrsim 6$ .

The discussion reported in Sect. 7.1 and 7.2, point out that, at least some of galaxy masses estimated in this work could suffer from large uncertainties associated to the simple assumptions at the base of the fitting method. Therefore, although  $M_{\text{BH}}$  estimates are strongly affected by the large (systematic) uncertainties associated to  $M_{\text{BH}}$  measurements at high- $z$  (up to  $\sim 0.4$  dex, see Sect. 5), we conclude that the observed  $M_{\text{BH}}/M_{\text{dyn}}$  values are also likely affected by uncertainties in  $M_{\text{dyn}}$ .

However, our method allowed us to obtain accurate galaxy dynamical mass estimates at such high redshift. We found that the spread in  $M_{\text{BH}}/M_{\text{dyn}}$  values at  $z \sim 4 - 7$  is much greater compared with that of local galaxies thus suggesting that the observed spread could not arise from the large uncertainties associated to rough galaxy (virial) mass estimates at high- $z$  usually adopted, but it could have a physical reason.

## 9. Discussion

In order to place our work in a larger context, we compare the prediction on BH-galaxy relation both from observational and

theoretical point of view. Then, we investigate observational biases possibly affecting the results and test the reliability of galaxy virial mass estimates.

In Sect. 9.1 we compare the  $M_{\text{BH}} - M_{\text{dyn}}$  and  $\Gamma - z$  relation presented in this work with other results on the high- $z$  BH-galaxy relation and we discuss the effect of observational biases.

In Sect. 9.2 we compare the prediction on BH-galaxy relation from recent simulations of galaxy evolution and we discuss potential issues on dynamical mass estimates at high redshift outlined from theoretical models.

Finally, in Sect. 9.3 we test the reliability of virial mass estimates by comparing them with the dynamical mass measurements.

### 9.1. Observational biases: comparison with other results on the early BH-galaxy relation

Previous works aimed to study the BH-host galaxy co-evolution in the early epochs show that  $z \gtrsim 6$  luminous quasars have BH to host galaxy mass ratio  $\sim 10$  times larger than the typical value observed in the local Universe implying that these SMBHs formed significantly earlier than their hosts (e.g., Walter et al. 2004; Maiolino 2009; Merloni et al. 2010; Decarli et al. 2010, 2018; Venemans et al. 2012, 2016; Wang et al. 2013, 2016; Trakhtenbrot et al. 2015). However these results may be affected by observational biases.

Because most luminous quasars are powered by the most massive BHs at high redshift, if there is a scatter in BH-host galaxy mass relation, for a given  $M_{\text{BH}}$ , the selection of objects with small galaxy mass is favoured due to the steepness of the galaxy mass function at its high-mass end (see e.g., Grazian et al. 2015; Song et al. 2016), thus producing an artificially high average  $M_{\text{BH}}/M_{\text{dyn}}$  (Lauer et al. 2007; Schulze & Wisotzki 2014). In order to investigate this selection bias effect, in Figure 11 we compare the distribution of our dynamical mass estimates, with the galaxy stellar mass function at different redshift. For this purpose, our dynamical mass measurements represent an upper limit

on the galaxy stellar mass. Most of the quasars are at the knee of the quasar luminosity function (Song et al. 2016), indicating that they represent the bulk of the quasar population at such high redshifts. On the other hand, J183+05, J167-13 and the most extreme J1319+0950 are at the massive-end of the  $M_*$ -function and they may be more affected by the "Lauer" bias. Notwithstanding all considerations on the reliability of dynamical mass estimates of the aforementioned objects, we can conclude that these three quasars may be considered the most evolved system known at  $z \sim 6$  in term of galaxy mass.

Interestingly, J167-13 together with J0923+0247 and J0129-0035 in our sample have a black hole mass  $M_{\text{BH}} < 5.0 \times 10^8 M_\odot$  (see Table 3) and all of them are consistent with the local BH-galaxy relation at  $z \sim 0$ . As discussed in Venemans et al. (2016), Wang et al. (2016) and Willott et al. (2015a, 2017); this may suggest that, while the  $z \sim 6$  quasars with BH masses on the order of  $10^8 M_\odot$  are close to the relation valid for their local counterpart, the most massive BHs ( $M_{\text{BH}} > 10^9 M_\odot$ ) at the earliest epochs grow faster than the quasar host galaxy and tend to be above the trend of local galaxies. This may imply that actually, there is no strong correlation between the two properties in high-redshift quasars, but that the scatter is much larger in the early Universe than today. However, to confirm this conclusion, a wide range of BH masses and larger sample is required to overcome the observational bias due to the intrinsic scatter of the BH-galaxy relation. In this context Izumi et al. (2018, 2019) studied the  $M_{\text{BH}} - M_{\text{dyn}}$  using a sample of seven  $z \gtrsim 6$  low luminosity quasars (absolute magnitude at  $1450\text{\AA}$ ,  $M_{1450} > -25$ ) targeted in [CII] $_{158\mu\text{m}}$  by ALMA. They derived the quasar host galaxy dynamical (virial) masses assuming rotating disc geometry and the axial ratio of [CII] flux map as proxy of the disc inclination angle. Furthermore they estimate  $M_{\text{BH}}$  through Single-Epoch virial relation or assuming Eddington-limited accretion. Izumi et al. (2018, 2019) results show that while the luminous quasars ( $M_{1450} < -25$ ) typically lie above the local relation (Kormendy & Ho 2013) with BH overmassive compared to local AGNs, the discrepancy becomes less evident at  $M_{\text{dyn}} \gtrsim 10^{11} M_\odot$  (see also e.g., Trakhtenbrot et al. 2017). On the other hand, most of the low-luminosity quasars show comparable or even lower ratios than the local one, particularly at a range of  $M_{\text{dyn}} \gtrsim 4 \times 10^{10} M_\odot$ . Therefore, Izumi et al. (2018, 2019) show that, at least in this high  $M_{\text{dyn}}$  range, previous works based on sample of luminous quasars might have been biased toward more massive black holes. If these results will be confirmed with future follow-up observations, the observed evolution of  $M_{\text{BH}}/M_{\text{dyn}}$  ratio out to  $z \sim 2 - 3$  could be explained as the result of sample selection bias only. However, the Izumi et al. (2018, 2019) work could be biased due to the use of virial masses. As we illustrate in Sect. 9.3, the galaxy masses estimated in this work through a full kinematical model, are not correlated with those estimated through virial theorem. This fact suggests that the use of galaxy virial mass in studying the BH-galaxy relation, could be reflected in an increasing scatter in the observed relation.

## 9.2. Comparison with recent theoretical models and simulations

The benchmark correlation in local galaxies are based on bulge stellar masses (Kormendy & Ho 2013). In high-redshift quasar the host galaxies are completely outshined by the central emission and the limited angular resolution of the current UV-based observations does not allow us to easily decouple the quasar

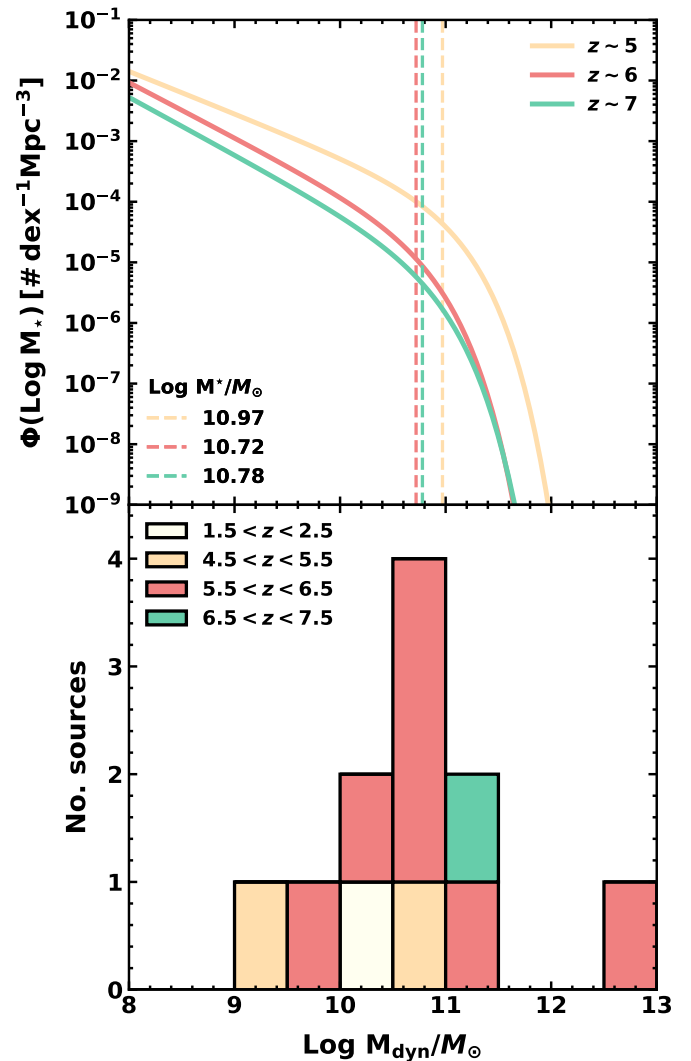


**Fig. 11.** Comparison between our dynamical mass measurements distribution and galaxy stellar mass function. *Upper panel:* Galaxy stellar mass function at different redshift (Song et al. 2016). The dashed vertical lines show the position of the  $M^*$  values that represent the "knee" of the mass function. *Lower panel:* Stacked histogram of our dynamical mass estimates.

from its host. Therefore, estimating the stellar mass content in galaxy out to  $z \sim 2-3$  is very challenging (see Sect. 1). However, at such high redshifts the galaxy bulges may not have formed yet or cannot be detected. Therefore, in the high redshift studies the dynamical mass of the host galaxy is estimated from the gas properties in the sub-mm observations and it is usually used as a proxy of bulge stellar mass.

Beyond the observational biases affecting these studies (see Sect. 9.1), recently Lupi et al. (2019) pointed out that the high- $z$  deviation from the local  $M_{\text{BH}} - M_{\text{dyn}}$  relation might be due to the different tracers used to estimate the mass of galaxies at high redshift, i.e. gas-based dynamical mass and the stellar mass. Lupi et al. (2019) performed an high resolution cosmological zoom-in simulation in order to investigate the evolution of quasar host by properly resolving both the distribution of the cold gas phase ( $30\text{ K} < T < 3000\text{ K}$ ) traced by [CII] $_{158\mu\text{m}}$  line emission, and stars traced by far-UV flux. Their results show that the gas settles in a well defined dense thin disc extending out to  $\sim 1\text{ kpc}$  already at  $z \sim 7$ . Adopting the techniques used in observational studies

they derive dynamical mass estimates through the virial theorem under the assumption of rotationally-supported systems. Comparing these dynamical (virial) mass estimates with the mass of the central BHs, they found an average BH-dynamical mass ratio of  $M_{\text{BH}}/M_{\text{dyn}} \sim 0.017$ , which is  $\sim 15$  times greater than local values (Decarli et al. 2010; Kormendy & Ho 2013; Reines & Volonteri 2015), in agreement with previous high- $z$  observations and simulations (see e.g., Walter et al. 2004; Venemans et al. 2017a; Barai et al. 2018; Decarli et al. 2018) and roughly consistent with our results. Additionally they also compare galaxy stellar mass with the central BH mass showing no sign of clear deviation with local relation (Reines & Volonteri 2015). This result implies that dynamical mass estimated by using the virial theorem underestimates the dynamical mass of the system. A similar discussion has been recently reported by Kohandel et al. (2019) who analysed the kinematical properties of a simulated star-forming galaxy at  $z \sim 7$ . They found that using the virial theorem in rotationally-supported system, the dynamical mass estimates suffer from large uncertainties depending on the disc inclination.

The approach proposed in our work, in which we perform a kinematical modelling of observed velocity fields, allow us to infer both disc inclination and dynamical mass so reducing the uncertainties and biases on our estimates. However, larger samples with higher angular resolution observations are required to finally assess whether a deviation from the local relation exists or not.

### 9.3. Comparison between virial masses and dynamical mass estimates

We test the reliability of virial mass estimates by comparing them with our dynamical mass measurements. For this purpose, we make rough dynamical (virial) mass ( $M_{\text{vir}}$ ) measurements of our galaxy sample following, e.g., Wang et al. (2013); Willott et al. (2015a); Decarli et al. (2018):

$$M_{\text{vir}} = G^{-1} R_{\text{em}} (0.75 \text{ FWHM}_{\text{line}} / \sin \beta)^2, \quad (8)$$

where  $R_{\text{em}}$  is the radius of the emitting region and  $\text{FWHM}_{\text{line}}$  is the full width at half maximum of the line emission.

We perform 2D Gaussian fits within CASA of the flux maps obtained in Sect. 3 and we estimate the deconvolved major ( $a_{\text{maj}}$ ) and minor axis ( $b_{\text{min}}$ ) of the best model. Then, we compute  $R_{\text{em}}$  as  $a_{\text{maj}}/2$  in physical length using the redshift estimates obtained in Sect. 3.1 and the disc inclination angle as  $\sin^2 \beta = 1 - (b_{\text{min}}/a_{\text{maj}})^2$ . Finally, we retrieve  $\text{FWHM}_{\text{line}}$  from the Gaussian fit of the line spectra (see Table A.1). The results of the 2D Gaussian fits, the  $R_{\text{em}}$  values and virial masses are listed in Table B.1.

In Figure 12 we compare dynamical virial masses estimated through Eq. 8 with the dynamical mass measurements obtained in this work through a full kinematical modelling (see Table 2).

We conclude that  $M_{\text{vir}}$  and  $M_{\text{dyn}}$  are roughly in good agreement but they appear not correlated confirming that virial mass is not reliable dynamical mass estimate of the host galaxy. Furthermore, we note that the errors on virial mass measurements are statistical errors, ignoring any intrinsic uncertainties and systematic biases associated to the virial assumption.

In order improve the galaxy virial mass estimate we can use the spectroastrometry method by Gnerucci et al. (2011). With this method is possible to probe spatial scales smaller than the angular resolution thus allowing a more accurate measure of the dimension of the line emitting region. On the other hand, the

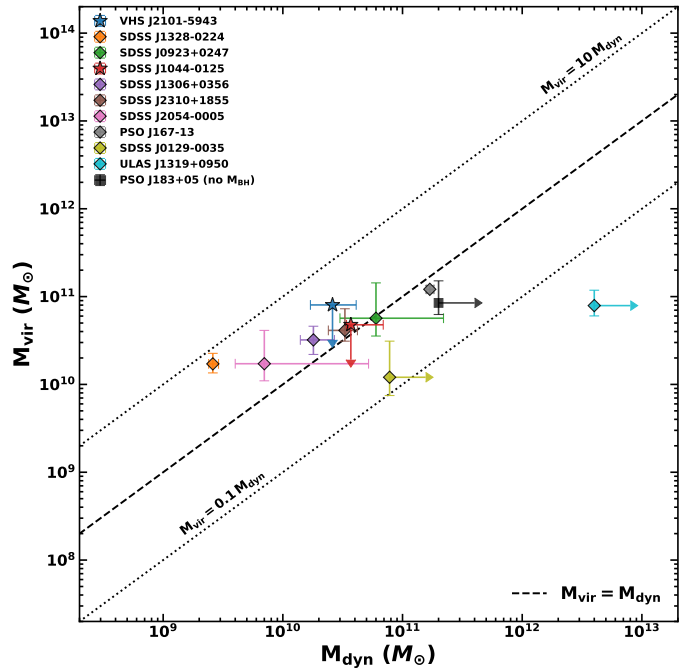


**Fig. 12.** Comparison between dynamical virial mass ( $M_{\text{vir}}$ ) computed using the flux map properties and dynamical mass ( $M_{\text{dyn}}$ ) obtained with the full kinematical model of the gas velocity field. The dashed line indicates the 1:1 relation, while dotted lines are 1 dex shifts. The objects represented with star symbols are upper limit on virial mass since their emission appear consistent with a point-like source (as a result of 2D Gaussian fits within CASA). In these cases, following Willott et al. (2015a) we assume  $\beta = 55$  deg as disc inclination angle. The black square indicates PSO J183-05 for which we retrieved a lower limit on  $M_{\text{dyn}}$  but for which  $M_{\text{BH}}$  is not available.

mass estimates are affected from uncertainties associated to the measure of galaxy disc inclination angle for which is possible to use the axial ratio from galaxy morphology. In Appendix C we compare the mass factor  $M_{\text{dyn}} \sin^2 \beta$  obtained through the full kinematical model, the virial formula and the spectroastrometry method. The results show that spectroastrometry is a robust proxy for the galaxy dynamical mass in contrast to the "classical" virial estimates usually adopted.

## 10. Conclusions

In this work we investigate the relation between supermassive black hole mass ( $M_{\text{BH}}$ ) and the dynamical mass of their host galaxies ( $M_{\text{dyn}}$ ) of a sample of 10 quasars at  $2.3 \lesssim z \lesssim 6.5$  targeted in either  $[\text{CII}]_{158\mu\text{m}}$  or CO rotational transitions by ALMA. We then studied the evolution of  $\Gamma = M_{\text{BH}}/M_{\text{gal}}$  across cosmic time.

Previous works exploiting ALMA observations have attempted to trace the  $M_{\text{BH}} - M_{\text{dyn}}$  relation at high- $z$  by estimating the galaxy mass through virial theorem and thus possibly introducing significant uncertainties and biases. To avoid such large uncertainties, we performed a kinematical modelling of the cold gas in the hosts taking into account the beam smearing effect.

Summarising we conclude that:

- The galaxy mass estimated using the virial theorem combining the axial ratio of flux map to estimate the disc inclination angle, and line FWHM as a proxy of circular velocity, suffer from large uncertainties and could underestimates the



dynamical mass of the system (Lupi et al. 2019; Kohandel et al. 2019).

- The beam smearing effect strongly affects the observed velocity field in the host galaxy making the disc inclination angle and galaxy dynamical mass almost degenerate parameters. This becomes more important decreasing the angular resolution and it should be taken into account in kinematical modelling.
- The dynamical masses estimated from the kinematical modelling highlight evidence of evolution of the  $M_{\text{BH}} - M_{\text{dyn}}$  relation consistently with previous works (e.g. Walter et al. 2004; McLure et al. 2006; Maiolino 2009; Bennert et al. 2010, 2011; Decarli et al. 2010, 2018; Merloni et al. 2010; Wang et al. 2010, 2013, 2016; Canalizo et al. 2012; Targett et al. 2012; Venemans et al. 2012, 2016, 2017b; Bongiorno et al. 2014; Trakhtenbrot et al. 2015). In particular, we conclude that, on average, our sample is placed above the reference relation found for galaxies in the local Universe. The normalisation  $\alpha$  of the BH-galaxy relation, is such that, on average, for a given value of  $M_{\text{dyn}}$ ,  $M_{\text{BH}}$  is  $\sim 10\times$  higher compared to that found by de Nicola et al. (2019) and  $\sim 150\times$  higher w.r.t. what Reines & Volonteri (2015) found using the total stellar mass of local AGNs.
- The ratio  $\Gamma = M_{\text{BH}}/M_{\text{dyn}}$  appears to be  $\sim 10\times$  the local value at  $z \sim 4 - 6$ , consistently with result found by Decarli et al. (2010) extrapolated up to  $z = 7$  excepting for four objects at  $z \sim 4 - 6$  that show  $\Gamma$  ratios consistent with the local one ( $\Gamma(z=0)$ ). Despite the low statistics this is the first evidence of a  $\Gamma$  value decreasing at  $z \sim 6$ . We are possibly witnessing the phase in which black hole rapidly grows with respect to the galaxy mass.
- The observed spread in  $M_{\text{BH}}/M_{\text{dyn}}$  values at  $z \sim 4 - 6$  is much greater compared to galaxies in the local Universe. Since the accurate galaxy dynamical mass estimates obtained in this work, the observed spread could be due to physical reasons and not associated to the large uncertainties affecting the galaxy virial mass estimates usually adopted in high- $z$  studies.
- The sources in our sample with  $M_{\text{BH}}$  on the order of  $10^8 M_{\odot}$  are close to the relation found for galaxies in the local Universe (Kormendy & Ho 2013; de Nicola et al. 2019), while the most massive BHs ( $M_{\text{BH}} > 10^9 M_{\odot}$ ) lie above them thus suggesting a faster evolution with respect to their host at  $z \sim 6$ .
- Most of our sample represents the bulk of the quasar population at  $z > 4$ ; thus, overall the selection of our galaxies sample are not strongly affected by the "Lauer" bias (Lauer et al. 2007; Schulze & Wisotzki 2014). However a wide range of BH masses and larger sample is required to be fully sample in order to avoid the observational bias due to the intrinsic scatter in the  $M_{\text{BH}} - M_{\text{dyn}}$  relation.

Based on our blind search, we conclude that one third of high- $z$  quasar hosts have gas kinematics consistent with rotating discs but it is still very challenging to infer the dynamical mass due to the poor angular resolution and sensitivity of current observations. The typical angular resolution of the observations ( $\sim 0.5''$ ) is frequently not good enough to constrain the dynamical parameters of the discs at  $z \gtrsim 5$  and the fitting procedures cannot take into account possible distortions of the velocity field introduced by instrumental effects. As a result, we inferred the dynamical masses only for 10 out of 72 quasars observed with ALMA so far.

On the other hand, for those quasars having deep ALMA observations and high angular resolution, this work showed that

dynamical mass estimations are feasible also at  $z \sim 6$ . Further ALMA high-angular resolution observations of high- $z$  quasars are crucial to study the evolution of  $M_{\text{BH}}/M_{\text{dyn}}$  ratio and verify whether  $\Gamma(z)$  decreases at  $z \gtrsim 6$  as suggest by our preliminary results.

*Acknowledgements.* We thank the anonymous referee for her/his careful reading of the manuscript and her/his comments which really helped us to improve the paper. We acknowledge the support from the LBT-Italian Coordination Facility for the execution of observations, data distribution and reduction. The LBT is an international collaboration among institutions in the United States, Italy and Germany. LBT Corporation partners are: The University of Arizona on behalf of the Arizona university system; Istituto Nazionale di Astrofisica, Italy; LBT Beteiligungsgesellschaft, Germany, representing the Max-Planck Society, the Astrophysical Institute Potsdam, and Heidelberg University; The Ohio State University, and The Research Corporation, on behalf of The University of Notre Dame, University of Minnesota, and University of Virginia. SC acknowledges support by the European Research Council No. 740120 'INTERSTELLAR'. MP is supported by the Programa Atracción de Talento de la Comunidad de Madrid via grant 2018-T2/TIC-11715. RM acknowledges supports by the Science and Technology Facilities Council (STFC) and from ERC Advanced Grant 695671 "QUENCH".

## References

- Asplund, M., Grevesse, N., Sauval, A. J., & Scott, P. 2009, *ARA&A*, 47, 481
- Banerji, M., Alaghband-Zadeh, S., Hewett, P. C., & McMahon, R. G. 2015, *MNRAS*, 447, 3368
- Banerji, M., Carilli, C. L., Jones, G., et al. 2017, *MNRAS*, 465, 4390
- Barai, P., Gallerani, S., Pallottini, A., et al. 2018, *MNRAS*, 473, 4003
- Begeman, K. G. 1987, PhD thesis, -
- Bennert, V. N., Auger, M. W., Treu, T., Woo, J.-H., & Malkan, M. A. 2011, *ApJ*, 742, 107
- Bennert, V. N., Treu, T., Woo, J.-H., et al. 2010, *ApJ*, 708, 1507
- Bentz, M. C., Peterson, B. M., Netzer, H., Pogge, R. W., & Vestergaard, M. 2009, *ApJ*, 697, 160
- Bentz, M. C., Peterson, B. M., Pogge, R. W., Vestergaard, M., & Onken, C. A. 2006, *ApJ*, 644, 133
- Binney, J. & Tremaine, S. 2008, *Galactic Dynamics: Second Edition*
- Bongiorno, A., Maiolino, R., Brusa, M., et al. 2014, *MNRAS*, 443, 2077
- Bosma, A. 1978, PhD thesis, -
- Brusa, M., Cresci, G., Daddi, E., et al. 2018, *A&A*, 612, A29
- Canalizo, G., Wold, M., Hiner, K. D., et al. 2012, *ApJ*, 760, 38
- Cappellari, M. & Emsellem, E. 2004, *PASP*, 116, 138
- Carilli, C. L. & Walter, F. 2013, *Annual Review of Astronomy and Astrophysics*, 51, 105
- Carniani, S., Gallerani, S., Vallini, L., et al. 2019, arXiv e-prints, arXiv:1902.01413
- Carniani, S., Marconi, A., Biggs, A., et al. 2013, *A&A*, 559, A29
- Carniani, S., Marconi, A., Maiolino, R., et al. 2017, *A&A*, 605, A105
- Coatman, L., Hewett, P. C., Banerji, M., et al. 2017, *MNRAS*, 465, 2120
- Cresci, G., Hicks, E. K. S., Genzel, R., et al. 2009, *ApJ*, 697, 115
- Cresci, G. & Maiolino, R. 2018, *Nature Astronomy*, 2, 179
- de Blok, W. J. G. & McGaugh, S. S. 1997, *MNRAS*, 290, 533
- De Loize, I., Cormier, D., Lebouteiller, V., et al. 2014, *A&A*, 568, A62
- de Nicola, S., Marconi, A., & Longo, G. 2019, *MNRAS*, 490, 600
- De Rosa, G., Decarli, R., Walter, F., et al. 2011, *ApJ*, 739, 56
- De Rosa, G., Venemans, B. P., Decarli, R., et al. 2014, *ApJ*, 790, 145
- Decarli, R., Dotti, M., Bañados, E., et al. 2019, arXiv e-prints, arXiv:1906.05308
- Decarli, R., Falomo, R., Treves, A., et al. 2010, *MNRAS*, 402, 2453
- Decarli, R., Walter, F., Venemans, B. P., et al. 2017, *Nature*, 545, 457
- Decarli, R., Walter, F., Venemans, B. P., et al. 2018, *ApJ*, 854, 97
- Denney, K. D. 2012, *ApJ*, 759, 44
- Di Matteo, T., Springel, V., & Hernquist, L. 2005, *Nature*, 433, 604
- Epinat, B., Amram, P., Balkowski, C., & Marcelin, M. 2010, *MNRAS*, 401, 2113
- Epinat, B., Contini, T., Le Fèvre, O., et al. 2009, *A&A*, 504, 789
- Feruglio, C., Fiore, F., Carniani, S., et al. 2018, *A&A*, 619, A39
- Flores, H., Hammer, F., Puech, M., Amram, P., & Balkowski, C. 2006, *A&A*, 455, 107
- Foreman-Mackey, D., Hogg, D. W., Lang, D., & Goodman, J. 2013, *Publications of the Astronomical Society of the Pacific*, 125, 306
- Freeman, K. C. 1970, *ApJ*, 160, 811
- Gallerani, S., Fan, X., Maiolino, R., & Pacucci, F. 2017, *PASA*, 34, e022
- Gnerucci, A., Marconi, A., Cresci, G., et al. 2011, *A&A*, 533, A124
- Grazian, A., Fontana, A., Santini, P., et al. 2015, *A&A*, 575, A96
- Grier, C. J., Shen, Y., Horne, K., et al. 2019, arXiv e-prints, arXiv:1904.03199
- Häring, N. & Rix, H.-W. 2004, *ApJ*, 604, L89

- Heckman, T. M. & Best, P. N. 2014, *ARA&A*, 52, 589
- Hinshaw, G., Larson, D., Komatsu, E., et al. 2013, *The Astrophysical Journal Supplement Series*, 208, 19
- Ho, L. C. 2007, *ApJ*, 669, 821
- Hopkins, P. F., Hernquist, L., Cox, T. J., & Kereš, D. 2008, *The Astrophysical Journal Supplement Series*, 175, 356
- Izumi, T., Onoue, M., Matsuoka, Y., et al. 2019, *arXiv e-prints*, arXiv:1904.07345
- Izumi, T., Onoue, M., Shirakata, H., et al. 2018, *PASJ*, 70, 36
- Jones, G. C., Carilli, C. L., Shao, Y., et al. 2017, *ApJ*, 850, 180
- Kakkad, D., Mainieri, V., Brusa, M., et al. 2017, *MNRAS*, 468, 4205
- Kamphuis, P., Józsa, G. I. G., Oh, S. H., et al. 2015, *MNRAS*, 452, 3139
- Kaspi, S., Brandt, W. N., Maoz, D., et al. 2007, *ApJ*, 659, 997
- Kaspi, S., Maoz, D., Netzer, H., et al. 2005, *ApJ*, 629, 61
- Kohandel, M., Pallottini, A., Ferrara, A., et al. 2019, *MNRAS*, 1423
- Kormendy, J. & Ho, L. C. 2013, *Annual Review of Astronomy and Astrophysics*, 51, 511
- Lamastra, A., Menci, N., Maiolino, R., Fiore, F., & Merloni, A. 2010, *MNRAS*, 405, 29
- Lauer, T. R., Tremaine, S., Richstone, D., & Faber, S. M. 2007, *ApJ*, 670, 249
- Lupi, A., Volonteri, M., Decarli, R., et al. 2019, *arXiv e-prints*, arXiv:1901.02464
- Magdis, G. E., Rigopoulou, D., Daddi, E., et al. 2017, *A&A*, 603, A93
- Maiolino, R. 2009, in *Astronomical Society of the Pacific Conference Series*, Vol. 408, *The Starburst-AGN Connection*, ed. W. Wang, Z. Yang, Z. Luo, & Z. Chen, 235
- Marconi, A. & Hunt, L. K. 2003, *ApJ*, 589, L21
- Mazzucchelli, C., Bañados, E., Venemans, B. P., et al. 2017, *ApJ*, 849, 91
- McGill, K. L., Woo, J.-H., Treu, T., & Malkan, M. A. 2008, *ApJ*, 673, 703
- McLure, R. J. & Dunlop, J. S. 2001, *MNRAS*, 327, 199
- McLure, R. J. & Dunlop, J. S. 2004, *MNRAS*, 352, 1390
- McLure, R. J. & Jarvis, M. J. 2002, *MNRAS*, 337, 109
- McLure, R. J., Jarvis, M. J., Targett, T. A., Dunlop, J. S., & Best, P. N. 2006, *MNRAS*, 368, 1395
- McMullin, J. P., Waters, B., Schiebel, D., Young, W., & Golap, K. 2007, in *Astronomical Data Analysis Software and Systems XVI*, Vol. 376, 127
- Menci, N., Fiore, F., Puccetti, S., & Cavaliere, A. 2008, *ApJ*, 686, 219
- Merloni, A., Bongiorno, A., Bolzonella, M., et al. 2010, *ApJ*, 708, 137
- Moré, J. J., Garbow, B. S., & Hillstom, K. E. 1980, *User guide for MINPACK-1*, Tech. Rep. ANL-80-74, Argonne Nat. Lab., Argonne, IL
- Neeleman, M., Bañados, E., Walter, F., et al. 2019, *arXiv e-prints*, arXiv:1907.02536
- O'Brien, J. C., Freeman, K. C., & van der Kruit, P. C. 2010, *A&A*, 515, A61
- Onken, C. A., Ferrarese, L., Merritt, D., et al. 2004, *ApJ*, 615, 645
- Park, D., Barth, A. J., Woo, J.-H., et al. 2017, *ApJ*, 839, 93
- Park, D., Woo, J.-H., Denney, K. D., & Shin, J. 2013, *ApJ*, 770, 87
- Peng, C. Y., Impey, C. D., Ho, L. C., Barton, E. J., & Rix, H.-W. 2006a, *ApJ*, 640, 114
- Peng, C. Y., Impey, C. D., Rix, H.-W., et al. 2006b, *ApJ*, 649, 616
- Perna, M., Sargent, M. T., Brusa, M., et al. 2018, *A&A*, 619, A90
- Popping, G., Decarli, R., Man, A. W. S., et al. 2017, *A&A*, 602, A11
- Portinari, L., Kotilainen, J., Falomo, R., & Decarli, R. 2012, *MNRAS*, 420, 732
- Reines, A. E. & Volonteri, M. 2015, *ApJ*, 813, 82
- Richards, G. T., Kruczek, N. E., Gallagher, S. C., et al. 2011, *AJ*, 141, 167
- Sani, E., Marconi, A., Hunt, L. K., & Risaliti, G. 2011, *MNRAS*, 413, 1479
- Saturni, F. G., Trevese, D., Vagnetti, F., Perna, M., & Dadina, M. 2016, *A&A*, 587, A43
- Schulze, A. & Wisotzki, L. 2014, *MNRAS*, 438, 3422
- Shao, Y., Wang, R., Jones, G. C., et al. 2017, *ApJ*, 845, 138
- Shen, Y., Greene, J. E., Strauss, M. A., Richards, G. T., & Schneider, D. P. 2008, *ApJ*, 680, 169
- Shen, Y., Richards, G. T., Strauss, M. A., et al. 2011, *ApJS*, 194, 45
- Shen, Y., Wu, J., Jiang, L., et al. 2019, *ApJ*, 873, 35
- Shields, G. A., Menezes, K. L., Massart, C. A., & Vand en Bout, P. 2006, *ApJ*, 641, 683
- Sijacki, D., Vogelsberger, M., Genel, S., et al. 2015, *MNRAS*, 452, 575
- Solomon, P. M. & Vanden Bout, P. A. 2005, *ARA&A*, 43, 677
- Soltan, A. 1982, *MNRAS*, 200, 115
- Song, M., Finkelstein, S. L., Ashby, M. L. N., et al. 2016, *ApJ*, 825, 5
- Swaters, R. A., Madore, B. F., & Trewheella, M. 2000, *ApJ*, 531, L107
- Swaters, R. A., Sancisi, R., van Albada, T. S., & van der Hulst, J. M. 2009, *A&A*, 493, 871
- Tacconi, L. J., Genzel, R., Saintonge, A., et al. 2018, *ApJ*, 853, 179
- Targett, T. A., Dunlop, J. S., & McLure, R. J. 2012, *MNRAS*, 420, 3621
- Taylor, E. N., Franx, M., Brinchmann, J., van der Wel, A., & van Dokkum, P. G. 2010, *ApJ*, 722, 1
- Trakhtenbrot, B., Lira, P., Netzer, H., et al. 2017, *ApJ*, 836, 8
- Trakhtenbrot, B., Netzer, H., Lira, P., & Shemmer, O. 2011, *ApJ*, 730, 7
- Trakhtenbrot, B., Urry, C. M., Civano, F., et al. 2015, *Science*, 349, 168
- Tremaine, S., Gebhardt, K., Bender, R., et al. 2002, *ApJ*, 574, 740
- Treu, T., Malkan, M. A., & Blandford, R. D. 2004, *ApJ*, 615, L97
- Treu, T., Woo, J.-H., Malkan, M. A., & Blandford, R. D. 2007, *ApJ*, 667, 117
- Trevese, D., Perna, M., Vagnetti, F., Saturni, F. G., & Dadina, M. 2014, *ApJ*, 795, 164
- Venemans, B. P., Bañados, E., Decarli, R., et al. 2015, *ApJ*, 801, L11
- Venemans, B. P., Decarli, R., Walter, F., et al. 2018, *ApJ*, 866, 159
- Venemans, B. P., McMahon, R. G., Walter, F., et al. 2012, *ApJ*, 751, L25
- Venemans, B. P., Neeleman, M., Walter, F., et al. 2019, *ApJ*, 874, L30
- Venemans, B. P., Walter, F., Decarli, R., et al. 2017a, *ApJ*, 851, L8
- Venemans, B. P., Walter, F., Decarli, R., et al. 2017b, *ApJ*, 837, 146
- Venemans, B. P., Walter, F., Decarli, R., et al. 2017c, *ApJ*, 845, 154
- Venemans, B. P., Walter, F., Zschaechner, L., et al. 2016, *ApJ*, 816, 37
- Vestergaard, M., Fan, X., Tremonti, C. A., Osmer, P. S., & Richards, G. T. 2008, *ApJ*, 674, L1
- Vestergaard, M. & Osmer, P. S. 2009, *ApJ*, 699, 800
- Vestergaard, M. & Peterson, B. M. 2006, *ApJ*, 641, 689
- Vietri, G., Piconcelli, E., Bischetti, M., et al. 2018, *A&A*, 617, A81
- Vignali, C., Piconcelli, E., Perna, M., et al. 2018, *MNRAS*, 477, 780
- Volonteri, M. & Reines, A. E. 2016, *ApJ*, 820, L6
- Volonteri, M. & Stark, D. P. 2011, *MNRAS*, 417, 2085
- Walter, F., Carilli, C., Bertoldi, F., et al. 2004, *ApJ*, 615, L17
- Wang, J.-G., Dong, X.-B., Wang, T.-G., et al. 2009, *ApJ*, 707, 1334
- Wang, R., Carilli, C. L., Neri, R., et al. 2010, *ApJ*, 714, 699
- Wang, R., Shao, Y., Carilli, C. L., et al. 2019, *arXiv e-prints*, arXiv:1904.07749
- Wang, R., Wagg, J., Carilli, C. L., et al. 2013, *ApJ*, 773, 44
- Wang, R., Wu, X.-B., Neri, R., et al. 2016, *ApJ*, 830, 53
- Weiner, B. J., Willmer, C. N. A., Faber, S. M., et al. 2006, *ApJ*, 653, 1027
- Willott, C. J., Albert, L., Arzoumanian, D., et al. 2010, *AJ*, 140, 546
- Willott, C. J., Bergeron, J., & Omont, A. 2015a, *ApJ*, 801, 123
- Willott, C. J., Bergeron, J., & Omont, A. 2017, *ApJ*, 850, 108
- Willott, C. J., Carilli, C. L., Wagg, J., & Wang, R. 2015b, *ApJ*, 807, 180
- Willott, C. J., Omont, A., & Bergeron, J. 2013, *ApJ*, 770, 13
- Woo, J.-H., Treu, T., Malkan, M. A., & Blandford, R. D. 2006, *ApJ*, 645, 900
- Woo, J.-H., Treu, T., Malkan, M. A., & Blandford, R. D. 2008, *ApJ*, 681, 925

## Appendix A: Integrated spectra: line properties and derived quantities

From the best-fit of the integrated spectra (see Sec. 3.1) we directly retrieve the line FWHM, and the velocity-integrated flux of the line ( $F_{line}$ ). Then, we also infer line luminosity ( $L_{line}$ ), [CII] mass ( $M_{[CII]}$ ), total gas mass ( $M_{gas}$ ), and [CII]-based star formation rate (SFR<sub>[CII]</sub>). The line luminosity can be computed following Solomon & Vanden Bout (2005):

$$L_{line} [L_{\odot}] = 1.04 \times 10^{-3} F_{line} v_{rest} (1+z)^{-1} D_L^2, \quad (A.1)$$

where  $F_{line}$  is in unit of  $Jy km s^{-1}$ ;  $v_{rest}$  in GHz and  $D_L$  in Mpc.

Then, in analogy with Venemans et al. (2017a), assuming optically thin [CII] emission and local thermodynamical equilibrium (LTE) of the carbon line, we estimate the mass of singly ionised carbon as:

$$\begin{aligned} M_{[CII]} [M_{\odot}] &= C m_C \frac{8\pi k_B v_{rest}^2}{hc^3 A_{ul}} Q(T_{ex}) \frac{1}{4} e^{91.2/T_{ex}} L'_{[CII]} \\ &= 2.92 \times 10^{-4} Q(T_{ex}) \frac{1}{4} e^{91.2/T_{ex}} L'_{[CII]}, \end{aligned} \quad (A.2)$$

where  $C$  is the conversion factor between  $pc^2$  and  $cm^2$ ,  $m_C$  the mass of a carbon atom,  $A_{ul} = 2.29 \times 10^{-6} s^{-1}$  the Einstein coefficient,  $Q(T_{ex}) = 2 + 4e^{-91.2/T_{ex}}$  the CII partition function, and  $T_{ex}$  the excitation temperature that we set equal to  $T_{ex} = 100$  K (see Venemans et al. 2017a). Then, assuming that all carbon atoms are singly ionised we also derive a lower limit on the total gas mass ( $M_{gas}$ ) using the carbon abundance relative to hydrogen atom (Asplund et al. 2009)  $M_C/M_H = 3.54 \times 10^{-3}$ . Finally we estimate the SFR using the SFR– $L_{[CII]}$  relations for high-redshift ( $z > 0.5$ ) galaxies from De Looze et al. (2014):

$$SFR_{[CII]} [M_{\odot} yr^{-1}] = 3.0 \times 10^{-9} (L_{[CII]}/L_{\odot})^{1.18} \quad (A.3)$$

with a systematic uncertainty of a factor of  $\sim 2.5$ . In Table A.1 we listed the results of spectral fits and the derived quantities for those sources with dynamical mass constrained. The reported quantities are consistent within  $\sim 2\sigma$  with estimates published in other works (e.g., Banerji et al. 2017; Wang et al. 2013; Decarli et al. 2017, 2018; Trakhtenbrot et al. 2017; Venemans et al. 2017c).

## Appendix B: Mass support from random motions

We investigate here the turbulent pressure support term, which arises from non-rotational motions, on the total dynamical mass of our QSO host galaxies (see e.g., Epinat et al. 2009; Taylor et al. 2010). This term is not taken into account in our disc model since the gas is circularly rotating in a thin disk.

Following Epinat et al. (2009) we quantify the mass supported by random motions inside the galaxy through the virial theorem:

$$M_{\sigma} = C \frac{\sigma_0^2 R_D}{G}, \quad (B.1)$$

where  $R_D$  is the scale radius of the exponential brightness profile (see Sect. 4);  $\sigma_0$  an estimate of constant velocity dispersion throughout the whole galaxy, and  $C$  is a parameter depending on the mass distribution and geometry. Here we assume  $C = 2.25$  that is the average value of known galactic mass distribution models (Binney & Tremaine 2008).

The intrinsic velocity dispersion can be estimated from the observed velocity dispersion map after taking into account the

angular and spectral resolution of observations. As a representative example, we choose SDSS J0923+0247. The velocity field of the latter shows a clear velocity gradient and we estimated the disc inclination of  $\sim 29$  deg and dynamical mass of  $\sim 6.0 \times 10^{11} M_{\odot}$  (see Fig. 7). Although our rotating thin disk model reproduces very well the observed velocity map, the observed velocity dispersion is slightly ( $\sim 1.4\times$ ) higher than what expected by our best-fit (see Fig. B.1). Indeed, the best-fitting velocity dispersion field includes only the effect of the unresolved velocity gradients and enlargement of emission line profile due to the beam smearing and the instrumental line-spread function (set to  $\sigma_{LSF} = 15 km s^{-1}$ ). As previously mentioned, our model does not include random motions due to the physics of the gas. The intrinsic velocity dispersion of the gas can be estimated by quadratically subtracting the model from the measured velocity dispersion map. The model and quadratic residuals are shown in Fig. B.1. Then, we computed the "1/errors"-weighted mean velocity dispersion ( $\sigma_0$ ), where the aforementioned errors are associated to the observed velocity dispersion values that are estimated from the spaxel-by-spaxel line fit of the data cube. The resulting value is  $\sigma_0 \sim 54 km s^{-1}$ . Using this value in the Eq. B.1 we obtain  $M_{\sigma} \sim 1.3 \times 10^9 M_{\odot}$ . This mass budget account for only  $\sim 2\%$  of the estimated dynamical mass obtained with kinematical modelling assuming rotating thin disc geometry. By comparing this value with the uncertainties on dynamical mass estimate ( $\sim 0.5$  dex), we conclude that the mass support from random motions is negligible in this system. We adopt the same technique for all the sources for which we obtained a dynamical mass estimate and verified that the eventual mass budget arising from random motions is always included within the dynamical mass uncertainties. Therefore we conclude that the rotating gas disk model provide a good description for the gas kinematics of our QSO host galaxies.

We stress that, for system that show complex or perturbed kinematics (e.g., due to the presence of outflow or a companion in the close environment of quasar, see Sect 7) the assumption of rotating disc geometry is undoubtedly less meaningful than for relaxed systems. This is the case of, e.g., SDSS J0129-0356, and ULAS J1319+0950, for which the best fits are consistent with face-on discs. On the other hand the observed velocity dispersion is still high ( $\sim 100 - 200 km s^{-1}$ , but consistent within  $2 - 3\sigma$  with the model) which is not expected for a face-on disc. Although these evidences support the fact that, at least in these extreme cases, the hypothesis of thin rotating disc is too simplified and the dynamical mass estimates should be considered tentative; deeper observations are needed in order to properly describe the kinematics in these complex system rather than a more accurate kinematical modelling of the current observations. However, our fitting method enables us to study the whole sample in a homogeneous way.

## Appendix C: Comparison between dynamical masses and the spectroastrometric mass estimates

Since the dynamical masses estimated in this work are measured through a full kinematical modelling of the velocity field, they can be considered a reliable mass estimates. Comparing them with mass measurements obtained with other methods enables to test the consistency of the results. In this section we compare the host galaxy dynamical mass measurements listed in Table 2, with the mass estimates obtained making use of the spectroastrometry



**Table A.1.** The key parameters and derived quantities estimated from the fits of integrated spectra.

No. <sup>a</sup>	Object ID	FWHM <sub>[CII]</sub> (km s <sup>-1</sup> )	$F_{[CII]}$ (Jy km s <sup>-1</sup> )	$L_{[CII]}$ (10 <sup>9</sup> L <sub>⊙</sub> )	$M_{[CII]}$ (10 <sup>6</sup> M <sub>⊙</sub> )	$M_{gas}$ (10 <sup>9</sup> M <sub>⊙</sub> )	SFR <sub>[CII]</sub> (M <sub>⊙</sub> yr <sup>-1</sup> )
2	VHS J2101-5943 <sup>†</sup>	222 <sup>+19</sup> <sub>-17</sub>	0.48 <sup>+0.04</sup> <sub>-0.04</sub>	0.019 <sup>+0.020</sup> <sub>-0.017</sub>			
6	SDSS J1328-0224	277 <sup>+24</sup> <sub>-22</sub>	2.43 <sup>+0.17</sup> <sub>-0.16</sub>	1.63 <sup>+0.11</sup> <sub>-0.11</sub>	4.3 <sup>+0.3</sup> <sub>-0.3</sub>	1.22 <sup>+0.08</sup> <sub>-0.08</sub>	223 <sup>+18</sup> <sub>-17</sub>
7	SDSS J0923+0247	328 <sup>+13</sup> <sub>-12</sub>	5.10 <sup>+0.18</sup> <sub>-0.18</sub>	3.44 <sup>+0.12</sup> <sub>-0.12</sub>	9.1 <sup>+0.3</sup> <sub>-0.3</sub>	2.58 <sup>+0.09</sup> <sub>-0.09</sub>	537 <sup>+22</sup> <sub>-22</sub>
9	SDSS J0129-0035	189 <sup>+9</sup> <sub>-9</sub>	2.14 <sup>+0.08</sup> <sub>-0.09</sub>	2.01 <sup>+0.08</sup> <sub>-0.08</sub>	5.3 <sup>+0.2</sup> <sub>-0.2</sub>	1.50 <sup>+0.06</sup> <sub>-0.06</sub>	284 <sup>+13</sup> <sub>-13</sub>
10	SDSS J1044-0125	422 <sup>+69</sup> <sub>-60</sub>	1.31 <sup>+0.19</sup> <sub>-0.19</sub>	1.23 <sup>+0.18</sup> <sub>-0.18</sub>	3.3 <sup>+0.5</sup> <sub>-0.5</sub>	0.92 <sup>+0.14</sup> <sub>-0.13</sub>	159 <sup>+28</sup> <sub>-27</sub>
11	SDSS J1306+0356	232 <sup>+28</sup> <sub>-24</sub>	2.4 <sup>+0.2</sup> <sub>-0.2</sub>	2.4 <sup>+0.2</sup> <sub>-0.2</sub>	6.3 <sup>+0.6</sup> <sub>-0.6</sub>	1.77 <sup>+0.16</sup> <sub>-0.16</sub>	346 <sup>+37</sup> <sub>-36</sub>
12	SDSS J2310+1855	381 <sup>+13</sup> <sub>-13</sub>	8.0 <sup>+0.2</sup> <sub>-0.2</sub>	7.9 <sup>+0.2</sup> <sub>-0.2</sub>	21.0 <sup>+0.6</sup> <sub>-0.6</sub>	5.92 <sup>+0.18</sup> <sub>-0.18</sub>	1434 <sup>+52</sup> <sub>-50</sub>
14	SDSS J2054-0005	243 <sup>+10</sup> <sub>-10</sub>	3.36 <sup>+0.12</sup> <sub>-0.12</sub>	3.36 <sup>+0.12</sup> <sub>-0.12</sub>	8.9 <sup>+0.3</sup> <sub>-0.3</sub>	2.51 <sup>+0.09</sup> <sub>-0.09</sub>	522 <sup>+23</sup> <sub>-22</sub>
19	ULAS J1319+0950	484 <sup>+33</sup> <sub>-30</sub>	2.60 <sup>+0.16</sup> <sub>-0.15</sub>	2.65 <sup>+0.16</sup> <sub>-0.16</sub>	7.0 <sup>+0.4</sup> <sub>-0.4</sub>	1.99 <sup>+0.12</sup> <sub>-0.12</sub>	395 <sup>+29</sup> <sub>-28</sub>
22	PSO J308-21	403 <sup>+35</sup> <sub>-33</sub>	1.03 <sup>+0.08</sup> <sub>-0.08</sub>	1.08 <sup>+0.08</sup> <sub>-0.08</sub>	2.7 <sup>+0.2</sup> <sub>-0.2</sub>	0.81 <sup>+0.06</sup> <sub>-0.06</sub>	137 <sup>+13</sup> <sub>-13</sub>
25	PSO J183+05	382 <sup>+19</sup> <sub>-17</sub>	5.1 <sup>+0.2</sup> <sub>-0.2</sub>	5.6 <sup>+0.2</sup> <sub>-0.2</sub>	14.8 <sup>+0.6</sup> <sub>-0.6</sub>	4.19 <sup>+0.17</sup> <sub>-0.17</sub>	954 <sup>+47</sup> <sub>-44</sub>
26	PSO J167-13	499 <sup>+17</sup> <sub>-17</sub>	3.20 <sup>+0.10</sup> <sub>-0.10</sub>	3.57 <sup>+0.11</sup> <sub>-0.11</sub>	9.5 <sup>+0.3</sup> <sub>-0.3</sub>	2.68 <sup>+0.08</sup> <sub>-0.08</sub>	562 <sup>+20</sup> <sub>-20</sub>
28	VIKING J0305-3150	245 <sup>+15</sup> <sub>-14</sub>	3.69 <sup>+0.19</sup> <sub>-0.18</sub>	4.2 <sup>+0.2</sup> <sub>-0.2</sub>	11.2 <sup>+0.6</sup> <sub>-0.5</sub>	3.15 <sup>+0.16</sup> <sub>-0.15</sub>	682 <sup>+41</sup> <sub>-38</sub>

**Notes.** <sup>a</sup>Identification numbers refer to that in Table 1. <sup>†</sup>This source is observed in CO(3-2). In this case FWHM and flux refer to this line. We thus do not derived the [CII]-based quantities for that.

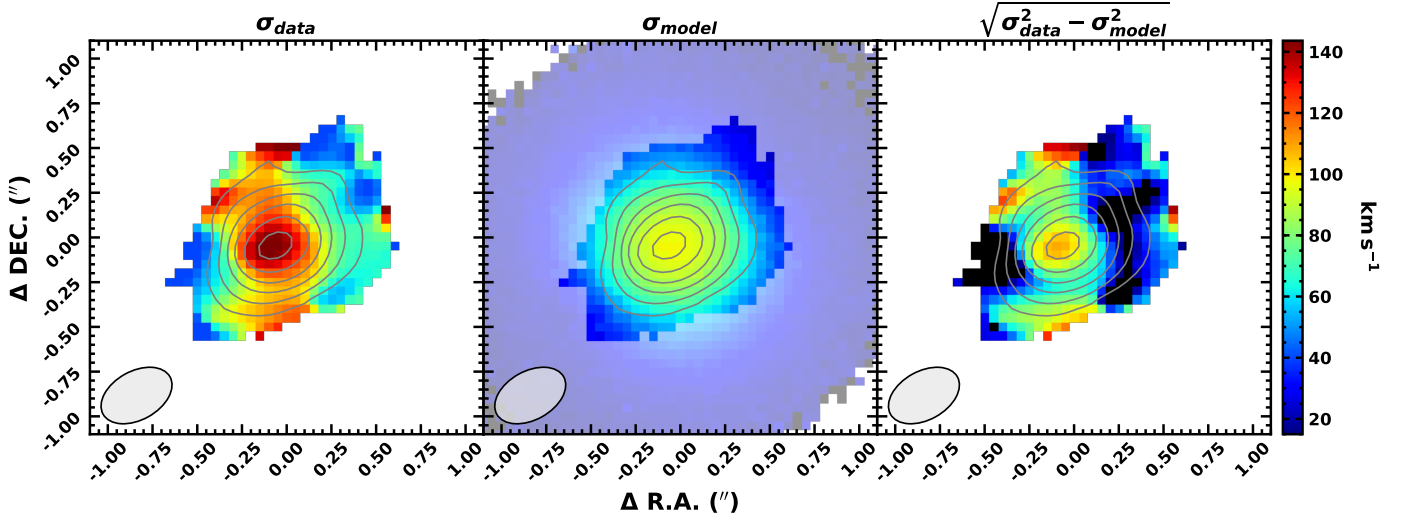


**Fig. B.1.** Estimation of local velocity dispersion in J0923+0247. *Left panel:* observed velocity dispersion field. *Central panel:* simulated flux-weighted velocity dispersion map along the line of sight, corresponding to the best fit model of the velocity field. *Right panel:* quadratic residuals showing representing the local velocity dispersion along the line of sight. The contours show the line-velocity integrated map. The contours correspond to  $[0.25I_0, 0.5I_0, I_0/e, 0.68I_0, 0.9I_0]$ , where  $I_0$  is the maximum value of the observed flux. At the left-bottom corner of each panel is shown the FWHM of the synthesised beam.

method by [Gnerucci et al. 2011](#) and the virial mass estimates obtained in Sect. 9.3.

Spectroastrometry is a technique which combines spatial and spectral resolution to probe spatial scales smaller than the angular resolution of the observations. We applied it to the case of our high- $z$  quasars sample to estimate the product  $\mu = M_{dyn} \sin^2 \beta$ . Following [Gnerucci et al. \(2011\)](#) we measure the FWHM and the central frequency of the line from the integrated spectra, (e.g., see Fig.3), then we collapse the redshifted and blueshifted channels obtaining "red" and "blue" maps respectively (see Fig. B.2). If the galaxy disc is at least marginally resolved, the latter two maps are spatially shifted due to the rotation of the gas. Then, we perform 2D fit of collapsed maps using an elliptical Gaus-

sian function and we determine the position of the two centroids. Thus, we compute the spectroastrometric radius ( $r_{spec}$ ), as the half distance between "red" and "blue" centroids. Finally, we use the FWHM and  $r_{spec}$  measurements and we estimate the spectroastrometric mass (see Eq. 2 in [Gnerucci et al. 2011](#)):

$$M_{spec} \sin^2 \beta = f_{spec} \mu_{spec} = f_{spec} \frac{FWHM_{line}^2 r_{spec}}{G} \quad (C.1)$$

where  $f_{spec}$  is the calibrator factor. Here we use the value by [Gnerucci et al. \(2011\)](#);  $f_{spec} = 1.0 \pm 0.1$ . The  $r_{spec}$  values and  $\mu_{spec}$  are listed in Table B.1.

In Fig. C.1 (upper panel) we compare  $\mu_{spec}$  from spectroastrometry with  $M_{dyn} \sin^2 \beta$  measured from the full kinematical

**Table B.1.** The parameters estimated from 2D Gaussian fit of the flux maps, virial mass estimates and the results of spectroastrometry method.

No. <sup>a</sup>	Object ID	FWHM <sub>major</sub> <sup>b</sup> (mas)	FWHM <sub>minor</sub> <sup>c</sup> (mas)	$R_{em}$ (kpc)	$M_{vir}$ ( $10^{10} M_{\odot}$ )	$r_{spec}$ (kpc)	$\mu_{spec}$ ( $10^{10} M_{\odot}$ )
2	VHS J2101-5943	POINT-LIKE SOURCE		< 8.34	< 8.0	< 2.3	< 2.6
6	SDSS J1328-0224	339 ± 50	189 ± 35	1.13 <sup>+0.17</sup> <sub>-0.17</sub>	1.7 <sup>+0.5</sup> <sub>-0.4</sub>	0.3 ± 0.2	0.5 ± 0.3
7	SDSS J0923+0247	385 ± 50	340 ± 58	1.28 <sup>+0.17</sup> <sub>-0.17</sub>	5.7 <sup>+8.7</sup> <sub>-2.1</sub>	0.7 ± 0.1	1.8 ± 0.4
9	SDSS J0129-0035	303 ± 51	271 ± 59	0.91 <sup>+0.15</sup> <sub>-0.15</sub>	1.2 <sup>+1.9</sup> <sub>-0.5</sub>	0.37 ± 0.06	0.30 ± 0.06
10	SDSS J1044-0125	POINT-LIKE SOURCE		< 1.38	< 4.8	0.4 ± 0.3	1.8 ± 1.5
11	SDSS J1306+0356	1290 ± 430	410 ± 240	3.8 <sup>+1.3</sup> <sub>-1.2</sub>	3.2 <sup>+1.4</sup> <sub>-1.0</sub>	1.1 ± 0.7	1.4 ± 0.9
12	SDSS J2310+1855	512 ± 61	287 ± 135	1.50 <sup>+0.18</sup> <sub>-0.18</sub>	4.1 <sup>+3.1</sup> <sub>-1.0</sub>	0.41 ± 0.07	1.4 ± 0.3
14	SDSS J2054-0005	352 ± 72	293 ± 97	1.0 <sup>+0.2</sup> <sub>-0.2</sub>	1.7 <sup>+2.4</sup> <sub>-0.6</sub>	0.33 ± 0.08	0.45 ± 0.12
19	ULAS J1319+0950	536 ± 95	328 ± 78	1.6 <sup>+0.3</sup> <sub>-0.3</sub>	7.9 <sup>+3.9</sup> <sub>-1.9</sub>	0.64 ± 0.12	3.5 ± 1.0
25	PSO J183+05	604 ± 63	477 ± 52	1.70 <sup>+0.18</sup> <sub>-0.18</sub>	8.5 <sup>+6.6</sup> <sub>-2.2</sub>	0.44 ± 0.12	1.5 ± 0.5
26	PSO J167-13	1068 ± 74	467 ± 53	3.0 <sup>+0.2</sup> <sub>-0.2</sub>	12.1 <sup>+1.2</sup> <sub>-1.1</sub>	1.16 ± 0.12	6.7 ± 1.0

**Notes.** <sup>a</sup>Identification numbers refer to that in Table 1. <sup>b,c</sup>Major and minor FWHM of the 2D best fit Gaussian of the flux maps deconvolved from the beam. Point-like source are explicitly indicated. In these cases, minor FWHM of the synthesised beam is taken as upper limit on the angular dimension of the emitting region. Uncertainties on quantities are statistical errors ignoring any possible systematic biases.

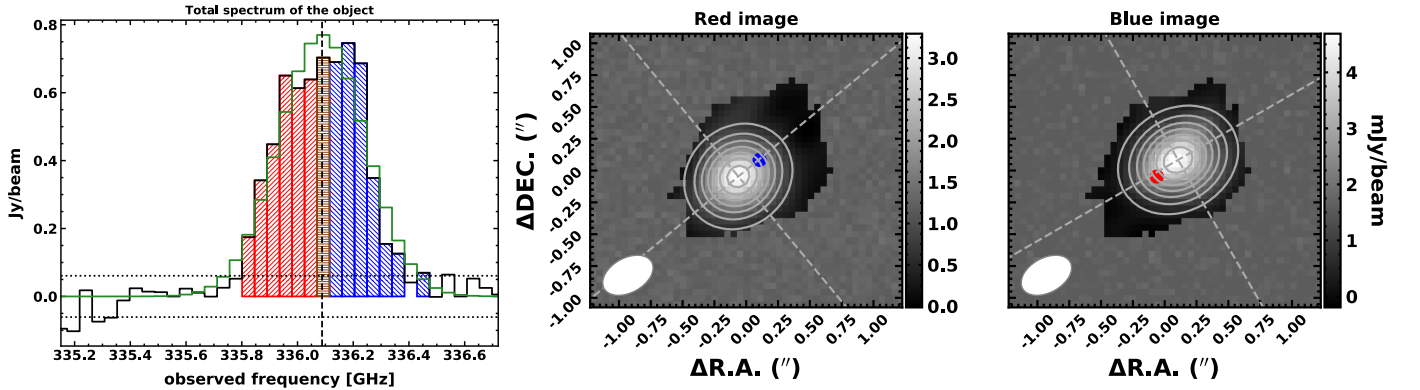


**Fig. B.2.** Integrated spectrum and red/blue maps of SDSS J0923+0247. *Left panel:* the data and the best fit model is shown with black and green line respectively. The red dashed vertical line indicates the central frequency; the rms of the residuals is indicated by the dotted horizontal lines. Channels used to create the red and blue maps (show on the right panels) are filled with their respective colours. The central brown bin is added to the red and blue side of the collapsed images with a weight given by the fraction of red and blue bins. *Right panels:* The best 2D Gaussian model is shown with white contours. The blue and red circle indicate the centroid positions of the counterpart map. Here, pixels not defined in the maps are replaced with simulated noise in order to avoid numerical drawbacks in the fitting process.

modelling (see Table 2). We conclude that the two estimators are consistent within uncertainties. We also compare  $\mu_{vir} = M_{vir} \sin^2 \beta$  from virial estimates (see Sect. 9.3) with  $M_{dyn} \sin^2 \beta$  (bottom panel of Fig. C.1). The results show that the virial mass factor  $\mu_{vir}$  and  $M_{dyn} \sin^2 \beta$  have a non-linear relation with large dispersion. Therefore, we conclude that the "classical" virial method does not provide a reliable prediction of  $M_{dyn} \sin^2 \beta$ . On the other hands, although also spectroastrometry method suffers from large uncertainties and biases, we conclude that  $\mu_{spec}$  are in better agreement with dynamical mass factor obtained with the full kinematical modelling of galaxy discs presented in this work. In fact, as discussed by Gnerucci et al. (2011) the "classical" virial mass estimate can be biased by systematic errors mostly associated to the measure of galaxy dimension.

This result confirms the reliability and usefulness of the spectroastrometry method especially in the case of poor spatial resolution and S/N ratio typical of majority of the current available high- $z$  galaxies observations.

## Appendix D: LBT observations and NIR spectra

The observations of the five quasars (SDSS J0129-0035, SDSS J2054-0005 and SDSS J2310+1855, PSO J308-21 and PSO J138+05) were executed between 2018 September and 2019 June (PI: G. Cresci) with LUCI in seeing limited conditions using the standard strategy for near-infrared long-slit spectroscopic observations: we dither the objects along the 1'' slit following an ABAB cycle in order to subtract the sky. We make use of the low resolution grating (G200,  $\lambda/\Delta\lambda \approx 2000$ ) and the N1.8 camera (pixel size  $\sim 0.25''/\text{pix}$ ) to maximise the signal-to-noise ratio. In order to obtain an accurate flux calibration of the spectra, needed to estimate  $L_{\lambda}$ , we also obtain images of the QSOs with the  $J$  or  $K$  filter with the N3.75 camera (pixel size  $\sim 0.12''/\text{pix}$ ). The total exposure time for spectroscopy is  $\sim 2$  hours per target and  $\sim 100, 200$  or  $800$  seconds for the imaging of the targets depending on their apparent magnitude. The data was reduced and delivered by LBT Imaging Data Center using the dedicated pipelines.

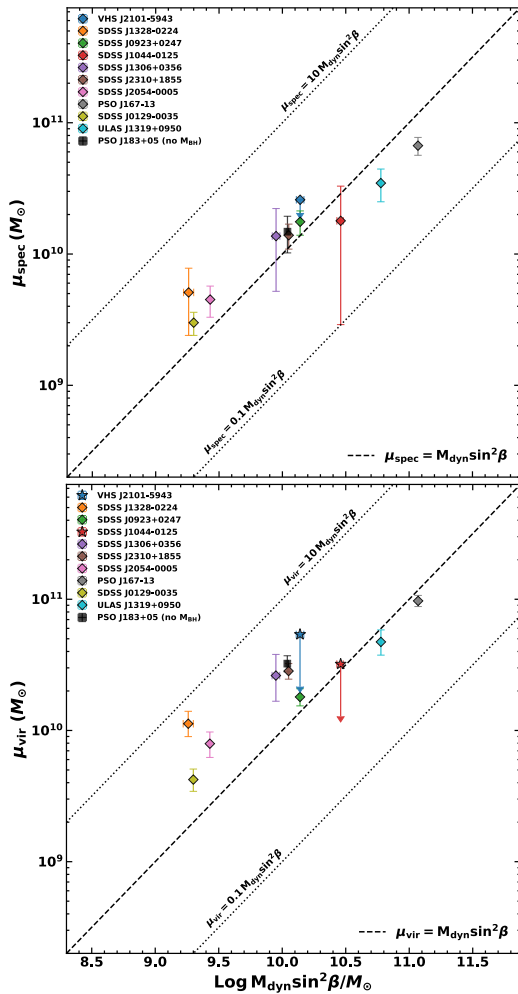


**Fig. C.1.** Comparison of galaxy mass factors obtained with spectroastrometry (*upper panel*) and virial estimates (*bottom panel*) with  $M_{\text{dyn}} \sin^2 \beta$  from full kinematical modelling of the host galaxy gas velocity field. The dashed black line represents the 1:1 relation. The object symbols are the same as in Fig. 12.

The requested time was derived assuming for the MgII line flux a typical value of  $5 \times 10^{-16} \text{ erg s}^{-1} \text{ cm}^{-2}$  at  $z \sim 6$  (Mazzuchelli et al. 2017), and for the CIV line a flux  $F_{\text{CIV}} \sim 3 \times F_{\text{MgII}}$  (Shen et al. 2011), and a line width of  $4000 \text{ km s}^{-1}$ .

Unfortunately we did not achieve the requested sensitivities due to bad weather conditions and we detected BLR emission only in J2310+1855. We therefore present here the  $M_{\text{BH}}$  mass of J2310+1855 derived from the observations of CIV BLR line. We also note that both Feruglio et al. (2018) and Shen et al. (2019) obtained independent NIR spectra of this target with different facilities. In particular Shen et al. (2019) published NIR spectra of a large sample  $z \sim 5.7$  QSOs, also providing a  $M_{\text{BH}}$  measurement for the J2310+1855 through virial relations based on CIV and MgII broad emission line.

Before modelling the CIV line in our LBT spectrum, we subtracted the continuum emission fitting a power law at both sides of the ionised carbon line (in the two windows at  $1450 \text{ \AA}$  and  $1700 \text{ \AA}$ ). Then, we use a single Gaussian model to reproduce the CIV BLR emission profile. In fact, the low SNR does not allow us to constrain the possible contribution from iron emission in the region around the CIV, which is expected to be negligible (see e.g., Shen et al. 2008, 2011), nor the possible emission from the CIV NLR line (e.g. Shen et al. 2011).

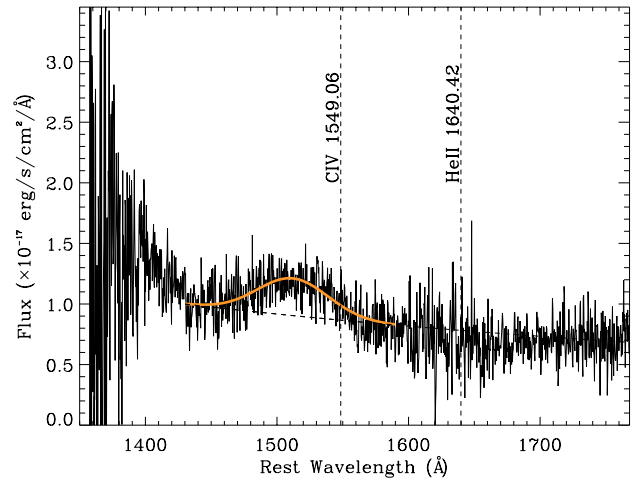


**Fig. D.1.** Portion of LBT/LUCI  $zJ$  spectrum of SDSS J2310+1855 around the CIV line which expected wavelength is indicated in the figure according to [CII]-based redshift. The orange and black dashed curve indicate the spectrum best-fit (line + continuum and continuum respectively).

From the best-fit of the CIV line, we derived a FWHM  $\sim 12500 \text{ km s}^{-1}$ , and from the extrapolated continuum at  $1350 \text{ \AA}$ , a flux of  $F_{1350} \sim 1.1 \times 10^{-17} \text{ erg s}^{-1} \text{ cm}^{-2} \text{ \AA}^{-1}$ , and a luminosity of  $\sim 10^{45.8} \text{ erg s}^{-1}$ . Using the Vestergaard & Peterson (2006) relation, we obtain  $\log M_{\text{BH}} \sim 9.8$ , consistently with Shen et al. (2019). The CIV line is blueshifted with respect to the [CII] $_{158\mu\text{m}}$  systemic of  $\Delta v \sim -7200 \text{ km s}^{-1}$ , strongly suggesting the presence of outflows in this source. We note that the values of FWHM and  $\Delta v$  of CIV broad line in J2310+1855 spectrum are consistent with the typical values estimated in high- $z$  QSOs (see e.g., Vietri et al. 2018). The CIV-based  $M_{\text{BH}}$  estimate can be therefore strongly biased; by adopting the different calibrations introduced to correct for the outflow contribution in CIV lines (see e.g. Vignali et al. 2018, and references therein), we obtain mass estimates in the range  $\log M_{\text{BH}} = 8.9 - 9.4$ , which is in agreement with the estimate by Feruglio et al. (2018). The uncertainties on these measurements are dominated by the intrinsic scatter ( $\approx 0.3$  dex; see e.g., Vestergaard & Peterson 2006; Denney 2012; Park et al. 2017) in the single-epoch calibrations, which is much larger than the typical uncertainties ascribed to the measurements of the line widths and fluxes.

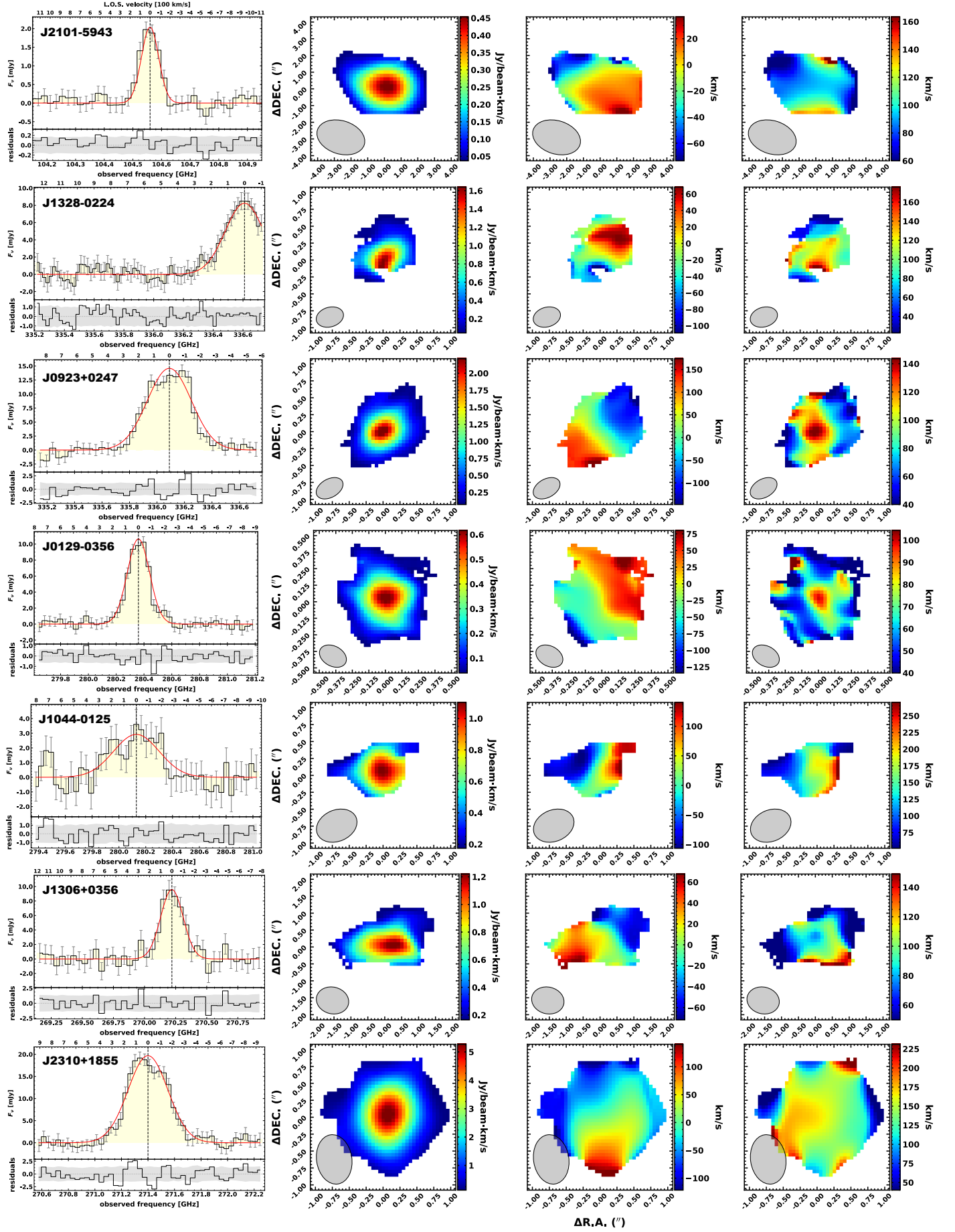
The latter values are consistent with the MgII-based  $M_{\text{BH}}$  reported in Shen et al. (2019), which has been used in this paper to study the  $M_{\text{BH}} - M_{\text{dyn}}$  relation. In Fig. D.1 we show the NIR spectrum of J2310+1855 with the best fit of CIV broad line.

## Appendix E: Maps, integrated spectra and the results of the kinematical modelling

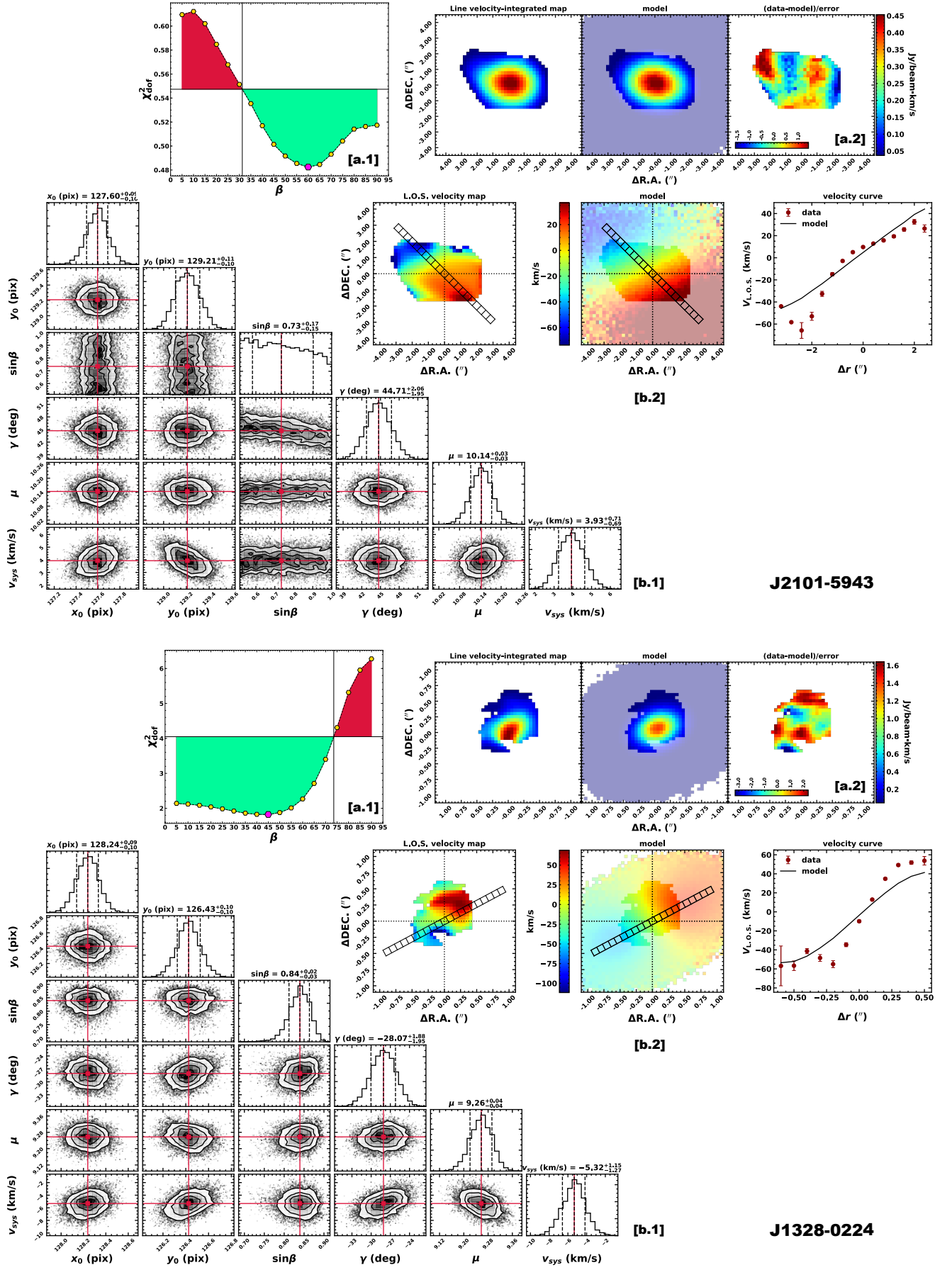
Here we report the integrated spectra, flux, velocity and velocity dispersion maps for objects in Table 2 (Fig. E.1). See Fig. 3 and Fig. 2 for the description of each panels.

We also report the 2D best fit of flux and velocity maps (Fig. E.2). The different panels are labelled as in Fig. 7, we refer to the latter for description of the figures.

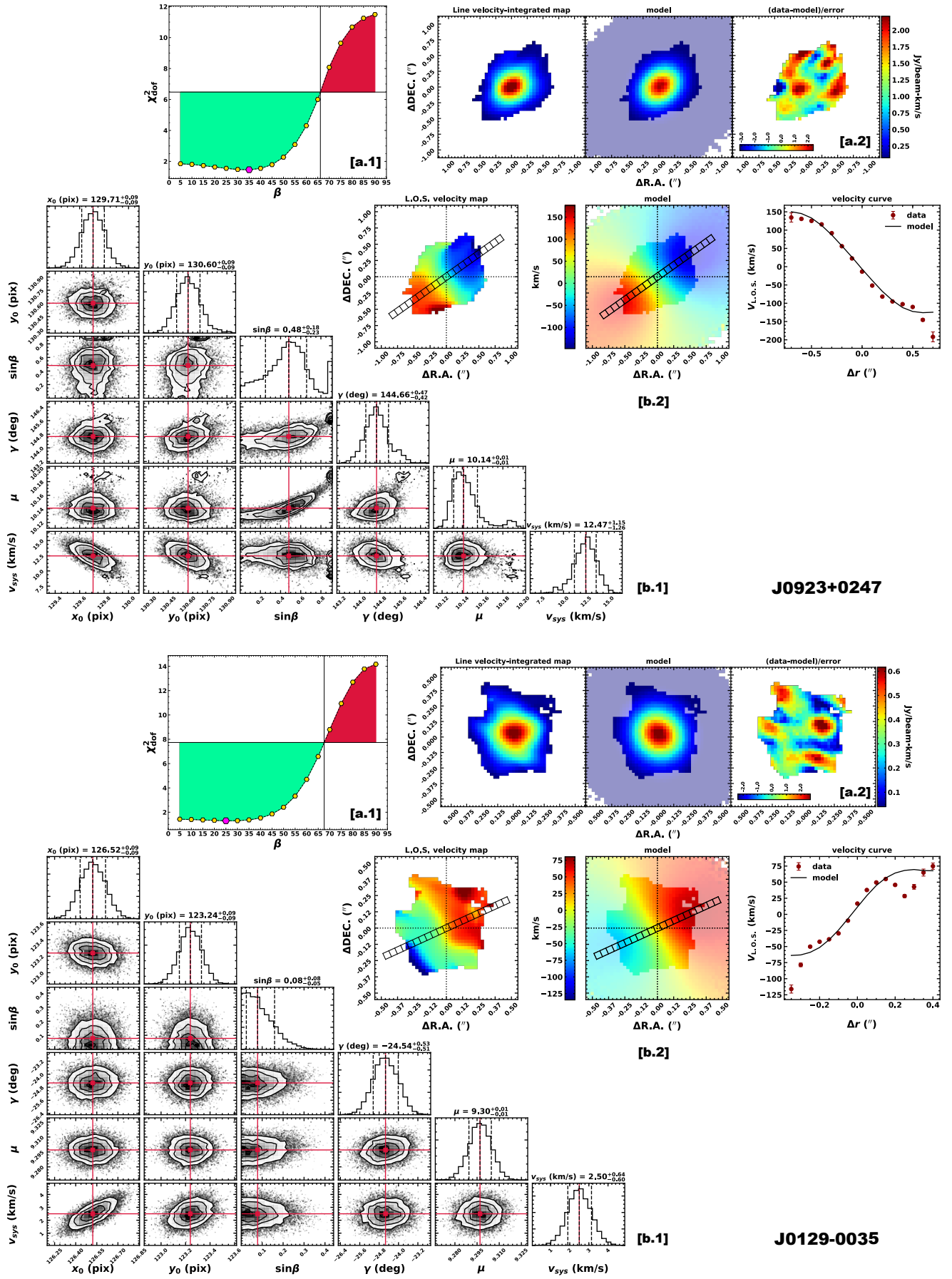


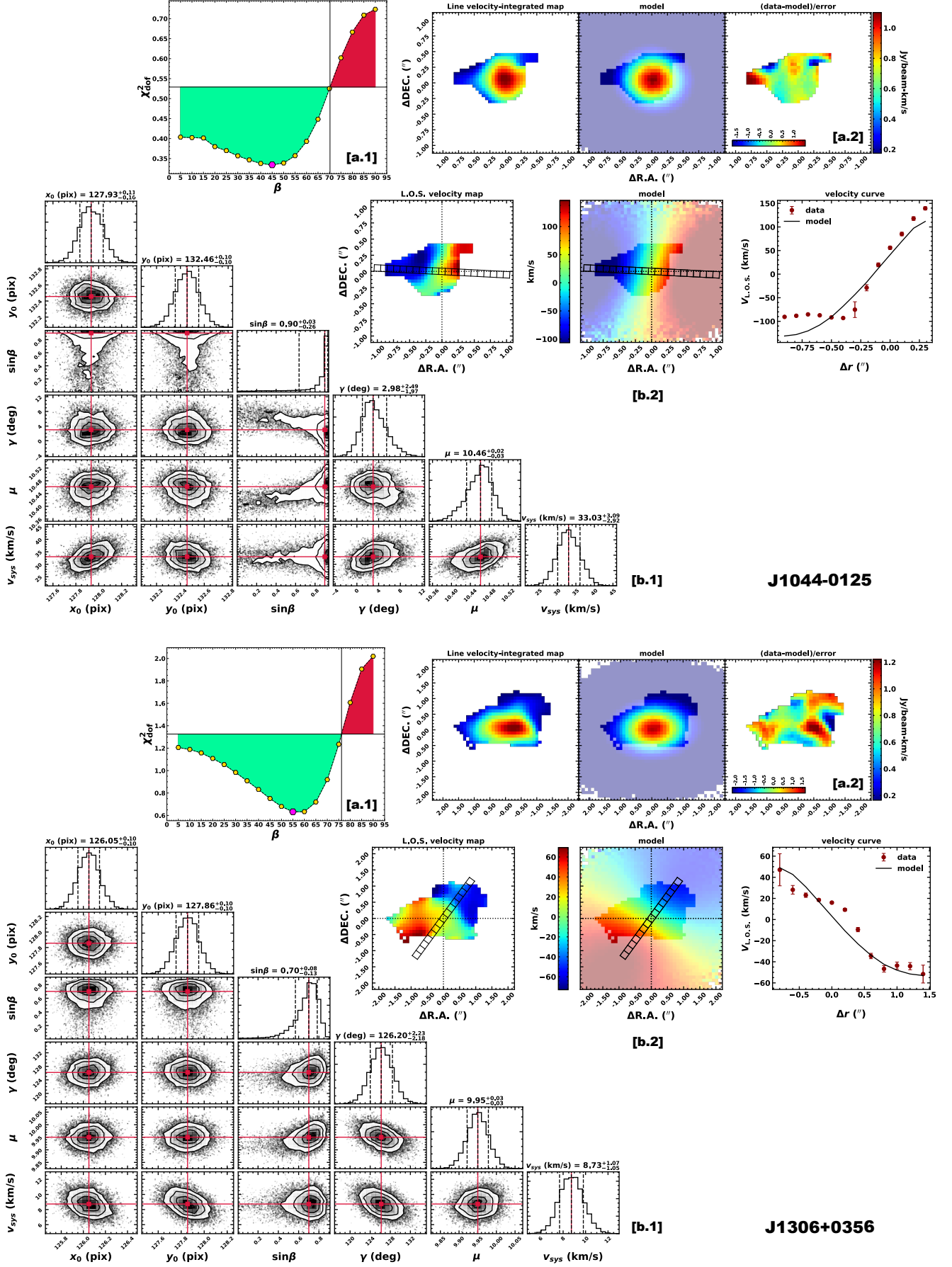


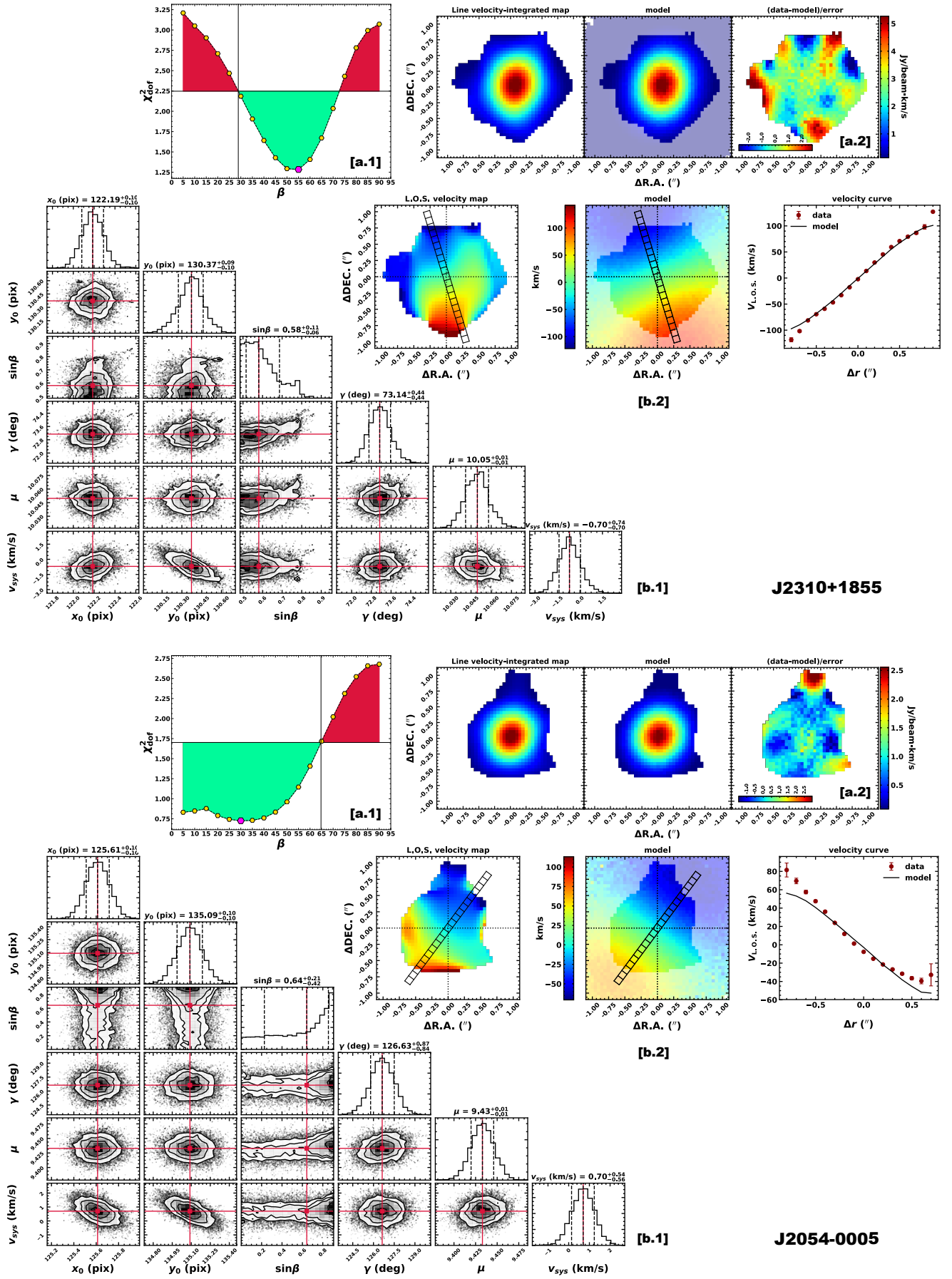




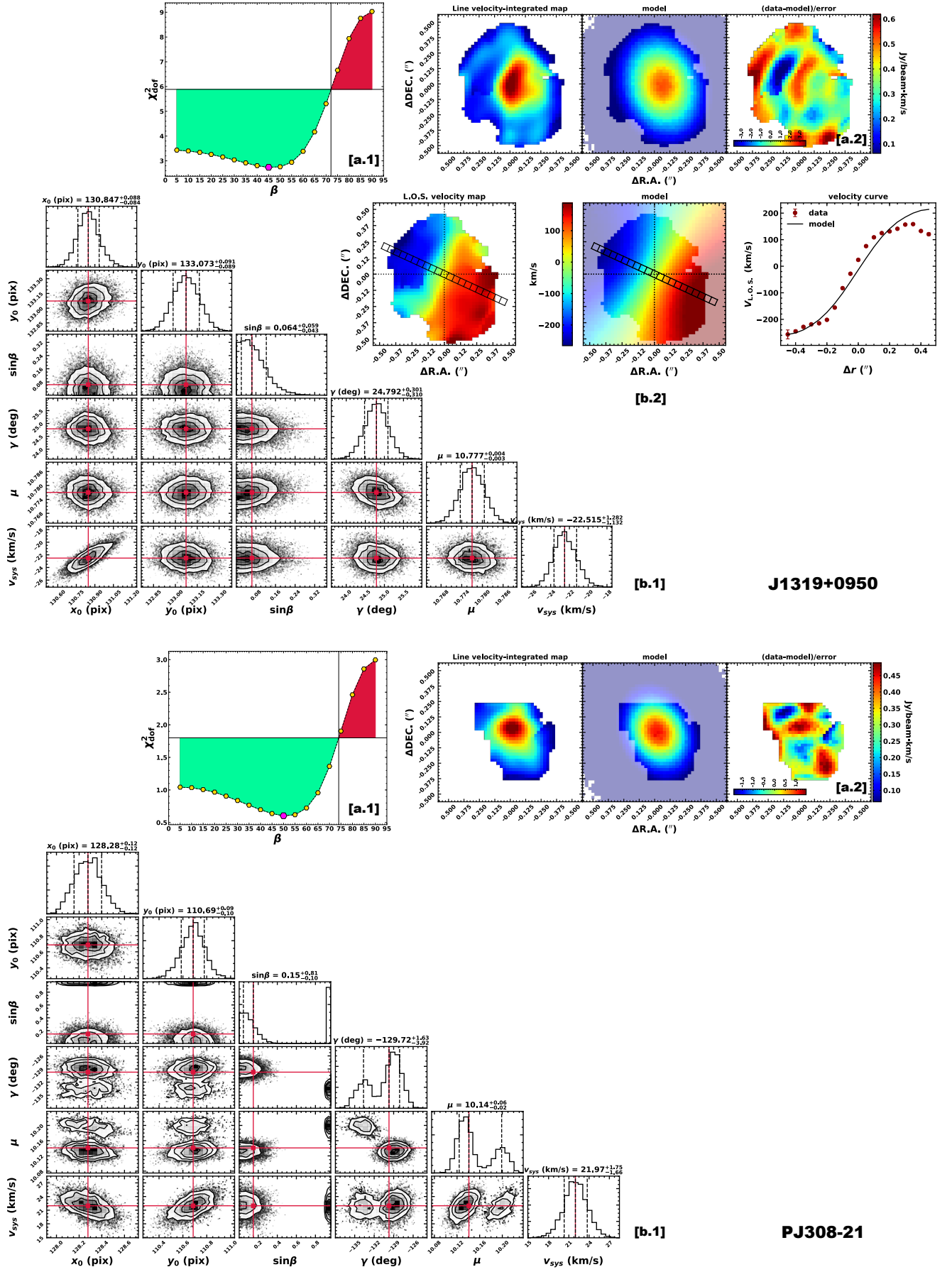


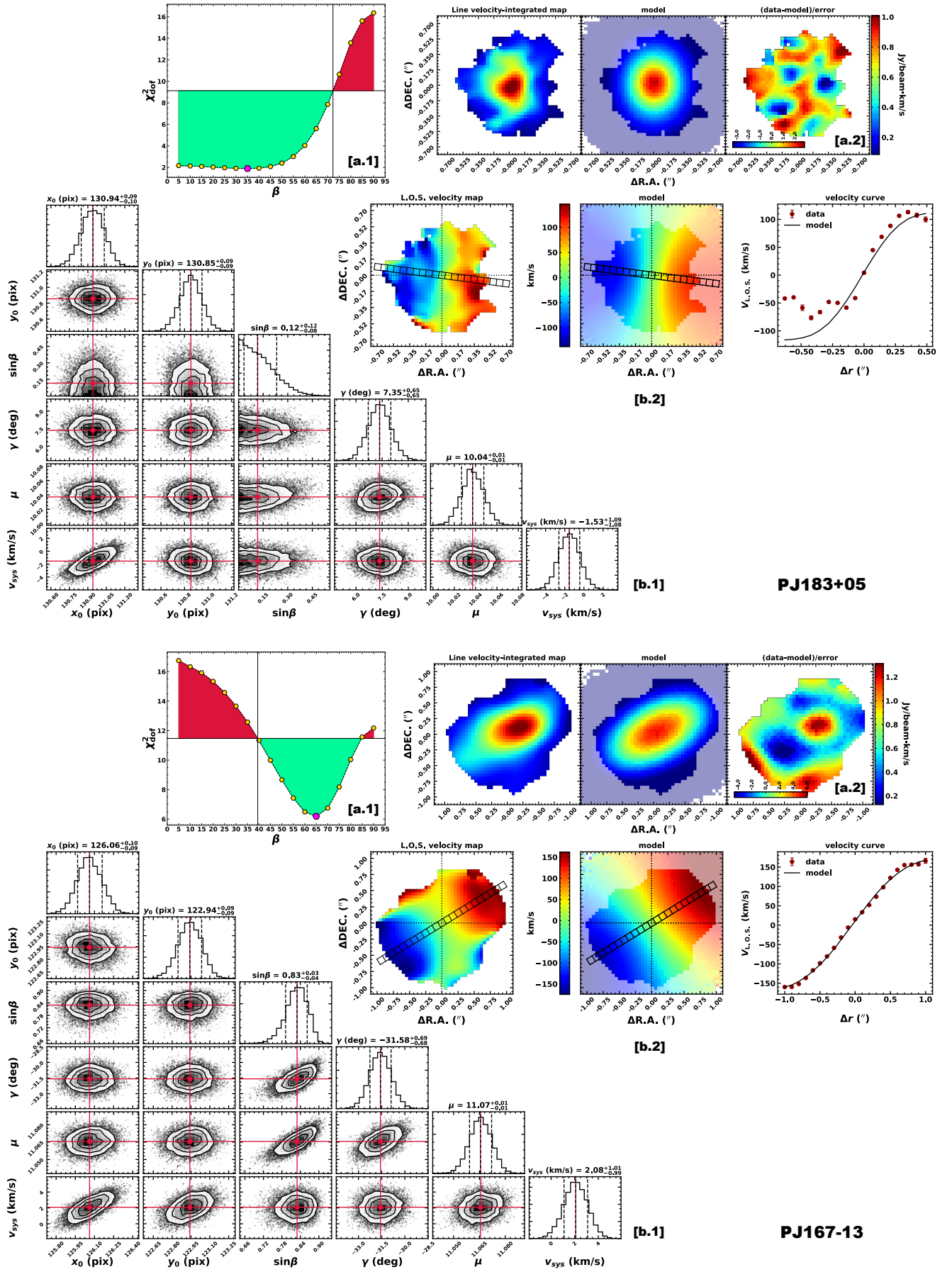


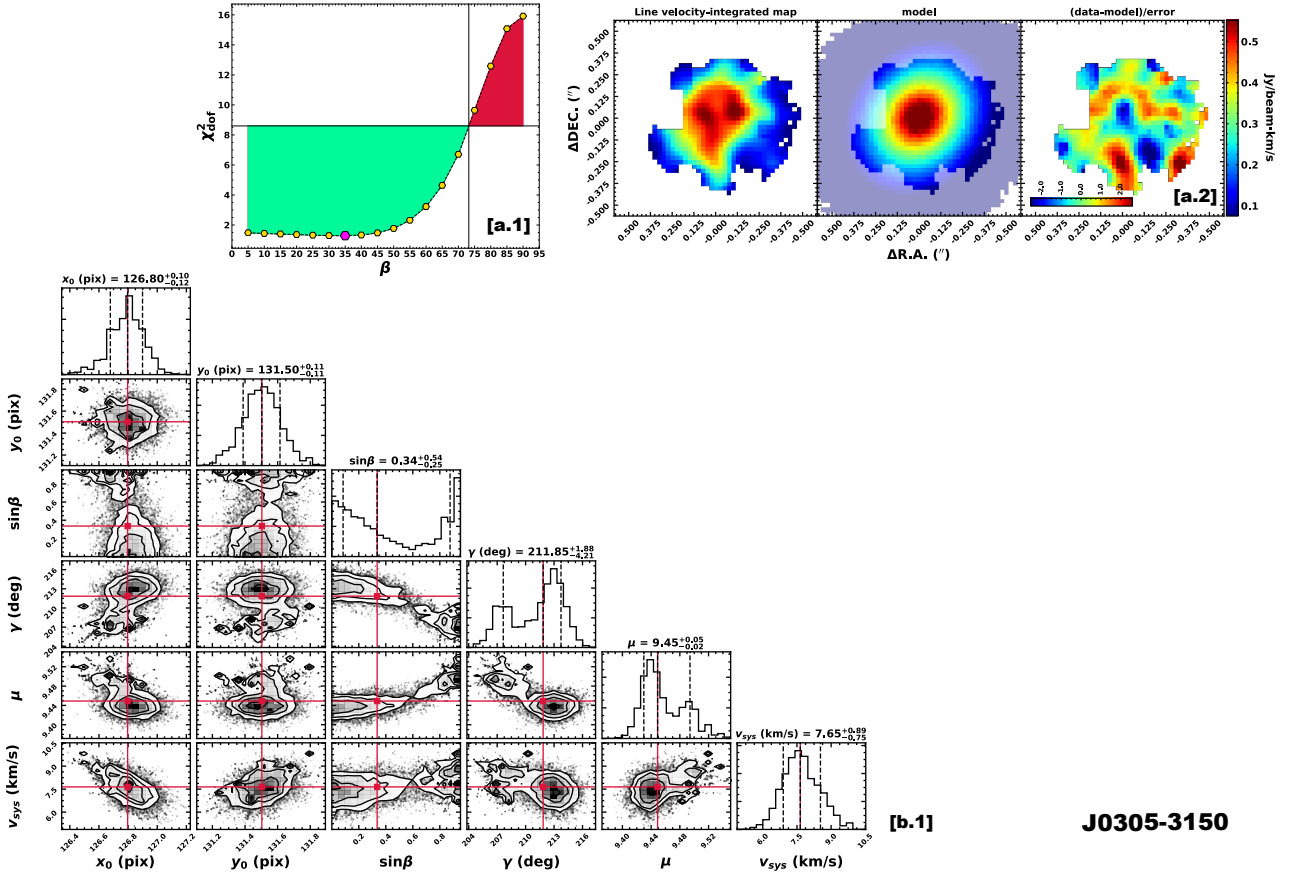












**Fig. E.2.** Results of 2D kinematical modelling for objects listed in Table 2. We refer to Fig. 7 for descriptions of individual panels.